

Synthesis of the Seismic Structure of the Greater Alaska Region: Continental Lithosphere

Xiaotao Yang¹, Michael Everett Mann², Karen Fischer², Margarete Jadamec^{3,4}, S. Shawn Wei⁵, Gary Pavlis⁶, and Andrew Schaeffer⁷

¹Department of Earth, Atmospheric, and Planetary Sciences, Purdue University, West Lafayette, IN,
USA.

²Department of Earth, Environmental, and Planetary Sciences, Brown University, Providence, Rhode
Island, USA.

³Department of Geology, University at Buffalo, SUNY, Buffalo, New York, USA.

⁴Institute for Artificial Intelligence and Data Science, University at Buffalo, SUNY, Buffalo, New York,
USA.

⁵Department of Earth and Environmental Sciences, Michigan State University, East Lansing, MI, USA.

⁶Department of Earth and Atmospheric Sciences, Indiana University Bloomington, Bloomington, IN,
USA.

⁷Geological Survey of Canada Pacific Division, Sidney Subdivision, Natural Resources Canada, Sidney,
BC, CA.

17 Abstract

18 Significant advances have been made over the last two decades in constraining the structure
19 of the continental lithosphere in Alaska, particularly with the EarthScope USArray seismic
20 data collection efforts. This paper distills recent seismic models in Alaska and western Yukon
21 (Canada) and relates them to major faults and tectonic terranes. We synthesize results from
22 eight shear-wave velocity models and seven crustal thickness models. Through objective
23 clustering of seismic velocity profiles, we identify six different velocity domains, separately
24 for the crust (at the depth range of 10-50 km) and the mantle (at the depth range of 40-120
25 km). The crustal seismic domains show strong correlations with average crustal thickness
26 patterns and the distribution of major faults and tectonic terranes. The mantle seismic
27 velocity domains demonstrate signatures of major faults and tectonic terranes in northern
28 Alaska while in southern Alaska the domains are primarily controlled by the geometry of
29 the subducting lithosphere. The results of this study have significant implications for the
30 tectonics and geodynamics of the overriding continental lithosphere from the margin to the
31 interior. This synthesis will be of interest to future studies of Alaska as well as other modern
32 and ancient systems involving convergent margins and terrane accretions.

33 **1 Introduction**

34 Geologic observations over the past 40 years suggest that the Alaskan lithosphere has
 35 been assembled from a collage of fragments since the Mesozoic (W. J. Nokleberg, MollStal-
 36 cup, et al., 1994; Plafker & Berg, 1994; Silberling et al., 1994; Colpron et al., 2007). These
 37 fragments make Alaska a type locality for the concept of terrane accretion (Coney et al.,
 38 1980; Colpron et al., 2007; Moore & Box, 2016; T. L. Pavlis et al., 2019). New seismic
 39 imaging results during the past two decades or so have provided fundamental constraints on
 40 the lithospheric structure of Alaska. In this study, we seek to shed new light on the struc-
 41 ture of the continental lithosphere in Alaska and northwesternmost Canada by integrating
 42 the results of recent shear-wave velocity models and receiver function studies enabled by
 43 data from the EarthScope Transportable Array (TA). In this paper, EarthScope refers to
 44 the U.S. National Science Foundation program operated from 2003 to 2018. Our study
 45 area lies within a broad tectonic region that spans the southern margin, where the Pacific
 46 plate subducts beneath the North American plate, northward to the interior and the North
 47 Slope of Alaska (Figure 1a). From west to east, this convergent margin transitions from
 48 ocean-ocean subduction approximately west of 166°W longitude (DeMets et al., 1994; Bird,
 49 2003; Tozer et al., 2019; Müller et al., 2019; Seton et al., 2020), through ocean-continent
 50 subduction between approximately 166°W to 144°W longitude (Plafker, Moore, & Winkler,
 51 1994; Bird, 2003; Jadamec & Billen, 2010; Tozer et al., 2019; Müller et al., 2019; Seton et
 52 al., 2020), to a subduction-collision zone from approximately 144°W to 137°W longitude
 53 (Enkelmann et al., 2010; Koons et al., 2010; Elliott & Freymueller, 2020). In northern
 54 Alaska, the overriding lithosphere transitions from continental to oceanic, through a mod-
 55 ern passive margin that leads into the Arctic Ocean and Canada Basin (Grantz et al., 1994;
 56 Tozer et al., 2019; Müller et al., 2019; Seton et al., 2020).

57 In this study, we focus on the lithosphere of mainland Alaska and the western Yukon
 58 region. This region is comprised of a series of amalgamated tectonic terranes (e.g., Plafker &
 59 Berg, 1994; Silberling et al., 1994; Colpron et al., 2007; Moore & Box, 2016) and large-scale
 60 relict and active faults (Fuis et al., 1991; W. J. Nokleberg, Plafker, & Wilson, 1994; Plafker,
 61 Gilpin, & Lahr, 1994; Eberhart-Phillips et al., 2003; Benowitz et al., 2022) (Figure 1b).
 62 Some of the major fault systems in the study area include the Kobuk Fault Zone along the
 63 southern border of the Brooks Range in northern Alaska, the Kaltag and Tintina Faults in
 64 central Alaska, and the Denali Fault System in southcentral Alaska (Plafker, Gilpin, & Lahr,
 65 1994). These faults are primarily parallel to the arcuate shape of the plate margin (Figure
 66 1b; Colpron et al., 2007). In addition, there are smaller-scale southwest-northeast trending
 67 faulting features, such as the Nixon Fork-Iditarod Fault and the Porcupine Shear Zone. For
 68 tectonic terranes, the Arctic Alaska terrane, with three subterranea, occupies most of the
 69 area north of the Kobuk Fault Zone and the Seward Peninsula. Western Alaska is dominated
 70 by the continental arc setting Koyukuk terrane and the accreted continental margin setting
 71 Farewell terrane (Figure 1b; Colpron et al., 2007). Eastern Alaska contains mostly the
 72 North America platformal and basinal terranes (Figure 1b; Colpron et al., 2007). The
 73 Wrangellia composite terrane dominates the Alaska region south of the Denali Fault System
 74 with accreted and displaced subterranea (Coney et al., 1980; Falkowski & Enkelmann, 2016).
 75 There are numerous first-order questions remaining regarding the structure and tectonics of
 76 the continental lithosphere in the Greater Alaska region. Given Alaska's history of terrane
 77 accretion, how do the terrane boundaries and related faults correlate with present-day crustal
 78 and mantle lithospheric structure? How strongly does the geologic history of a terrane
 79 control its present-day crustal structure? How deep do the signatures of terrane accretion
 80 extend into the mantle lithosphere? What is the impact of the subducting-colliding Yakutat
 81 Microplate on the structure of the overriding plate?

82 The new data from the EarthScope TA, together with other concurrent temporary
 83 seismic networks, have provided new constraints on the seismic and tectonic structure of
 84 the continental United States and Alaska. From 2005 to 2015 the TA was deployed across
 85 the contiguous United States from the active tectonic boundary in the west to the passive

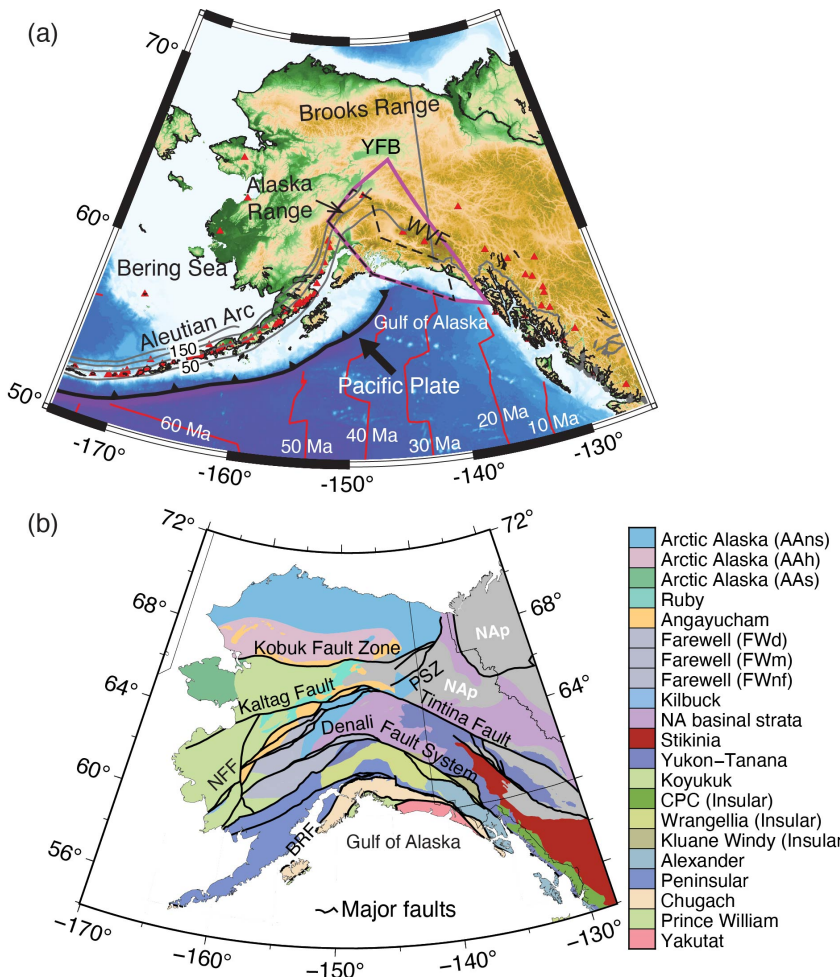


Figure 1. Tectonic settings of Alaska. (a) Key tectonic settings of Alaska, including the subduction of the Pacific Plate and the Yakutat microplate along the curved margin. Major topographic features are labeled, including the Alaska Range, the Brooks Range, the Yukon Flats Basin (YFB), and the Wrangell Volcanic Field (WVF). The slab depth contours are from Slab2.0 (Hayes et al., 2018). The ages of the Pacific Plate are from Seton et al. (2020). The dashed black and solid magenta polygons mark the outlines of the Yakutat Microplate proposed by Eberhart-Phillips et al. (2004) and G. L. Pavlis et al. (2019), respectively. Red triangles are active volcanoes. (b) Major terranes (color-shaded areas) and faults (thick lines) of the Canadian-Alaskan cordillera from Colpron et al. (2007). Fault labels: PSZ - Porcupine Shear Zone, NFF - Nixon Fork-Iditarod Fault, BRF - Border Range Fault. Terrane labels: AAns - Arctic Alaska North Slope subterrane, AAh - Arctic Alaska Hammond-Coldfoot subterrane, AAs - Arctic Alaska Seward subterrane, FWd - Farewell Dillinger subterrane, FWm - Farewell Mystic subterrane, FWnf - Farewell Nixon Fork subterrane, CPC - Coast Plutonic Complex, NAp - North America platformal strata in western Laurentia.

86 continental margin on the east coast. In 2015, the USArray Transportable Array began
 87 moving instruments to Alaska and westernmost Canada. This has dramatically improved
 88 the seismic data coverage in Alaska and western Yukon (Canada). In this paper, we present
 89 a synthesis of seismic studies that have benefited from EarthScope data, focusing on new
 90 constraints these results have given on the seismic structure of the lithosphere of the region.

91 By combining eight shear-wave velocity models and seven crustal thickness models, we iden-
 92 tify six different seismic domains, separately for the crust (at the depth range of 10-50 km)
 93 and the mantle lithosphere (at the depth range of 40-120 km). The crustal seismic domains
 94 show strong correlations with major faults and tectonic terranes. The mantle seismic do-
 95 mains demonstrate signatures of major faults and tectonic terranes in northern Alaska with
 96 a prominent reflection of the subduction structure in central and southern Alaska. The
 97 results of this study have significant implications for the tectonics and geodynamics of the
 98 overriding continental lithosphere from the margin to the interior.

99 2 Data: compilation of seismic models

100 The study area spans the region from the subduction zone along the southern Alaska
 101 margin to the North Slope of Alaska bordering the Arctic Ocean. We focus on two types
 102 of seismic results for Alaska: 1) 3-D shear-wave velocity models of the crust and uppermost
 103 mantle, and 2) thicknesses of the overriding crust. We exclude results that only cover
 104 the footprint of the Alaska Amphibious Community Seismic Experiment (Barcheck et al.,
 105 2020). We attempt to reveal common features in the models we used but not to compare
 106 and contrast detailed interpretations different authors made from their individual models.
 107 The readers are encouraged to read the corresponding publications summarized in Tables 1
 108 and 2 for detailed descriptions of each individual seismic model we used. The seismic models
 109 synthesized in this study benefit from the data recorded by 29 seismic networks, as shown
 110 in Figure 2a. The network codes include 5C, 7C, AK, AT, AV, CN, II, IM, IU, PN, PO,
 111 PP, TA, US, XE, XF, XL, XM, XN, XO, XR, XV, XY, XZ, YE, YG, YM, YO, YV, Z5,
 112 and ZE. See **Availability Statement** and Table S1 in the supplement for the descriptions
 113 and references corresponding to these network codes.

114 2.1 3-D shear-wave velocity models

115 We collected eight representative 3-D shear-wave velocity models. Since the arrival of
 116 the EarthScope TA in Alaska, there have been a large number of velocity models published
 117 using data from the EarthScope TA stations and the Alaska regional network stations (e.g.,
 118 Ward & Lin, 2018; Jiang et al., 2018; Martin-Short et al., 2018; Gou et al., 2019; Feng &
 119 Ritzwoller, 2019; Berg et al., 2020; Yang & Gao, 2020; Esteve et al., 2020; Audet et al., 2019;
 120 Nayak et al., 2020; Esteve et al., 2021; Gama et al., 2022b; Liu et al., 2022). To narrow
 121 down the velocity models for this synthesis work, we select velocity models that satisfy
 122 the following conditions: 1) covers most of mainland Alaska, 2) provides isotropic seismic
 123 velocities, 3) uses part or all EarthScope TA data, 4) includes surface wave data to aid with
 124 the vertical resolution, 5) is available as a digital velocity model through IRIS Earth Model
 125 Collaboration or personal communications, 6) provides absolute velocities or perturbations
 126 with an explicitly known reference model, and 7) covers at least the continental crust in
 127 depth. With these criteria, we choose eight 3-D shear-wave velocity models using different
 128 datasets and imaging methods. The data types and tomographic imaging methods for all
 129 selected models are summarized in Table 1. Hereafter, we refer to these models with the
 130 labels as in Table 1. For simplicity and consistency in descriptions, we label each of the
 131 velocity models systematically with the initial of the last name of the first author and the
 132 year the model was published.

133 The footprint of these stations covers the entire mainland Alaska region and the western
 134 Yukon (Canada) region. The EarthScope TA stations have a nominal spacing of about 85
 135 km, while some places, such as central Alaska and the Wrangell Volcanic Field, are covered
 136 with denser regional arrays. Among the eight velocity models, the Y2020 model (Yang &
 137 Gao, 2020) covers only central and southern Alaska (Figure 2b) while the M2018 (Martin-
 138 Short et al., 2018) and G2022 (Gama et al., 2022b) models cover most of Alaska. The rest
 139 of the velocity models cover the entire Alaska region. The J2018 (Jiang et al., 2018), F2019
 140 (Feng & Ritzwoller, 2019), B2020 (Berg et al., 2020), and N2020 (Nayak et al., 2020) models

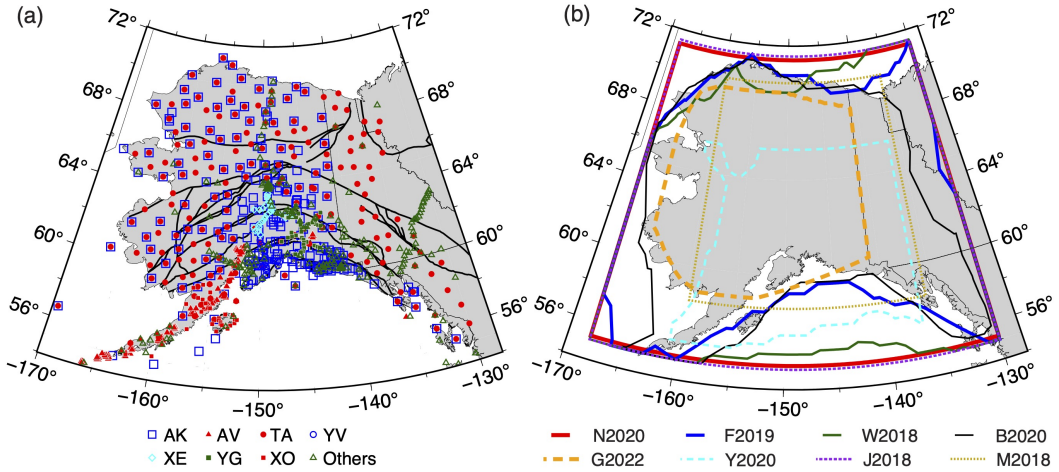


Figure 2. Seismic stations in Alaska and coverage of the seismic velocity models synthesized in this study. (a) Seismic stations from 29 networks between 2000 and 2022 that are used by the synthesized seismic models in this study. The station information is available through the IRIS Data Management Center and the International Federation of Digital Seismograph Networks. For simplicity in plotting, we plot the top seven networks, with the most stations, using different colors and symbols. Please see Table S1 in the supplement for the descriptions and references of all seismic networks plotted here. The thick lines are major fault traces as in Figure 1b. (b) Outlines of the shear-wave velocity models that are defined as regions with available shear-wave velocities between 1 km/s and 6 km/s. We use this velocity range to exclude unconstrained model grids. The outlines are estimated using the velocity model at the depth of about 30 km for all models. W2018 - model by Ward and Lin (2018), J2018 - model by Jiang et al. (2018), M2018 - model by Martin-Short et al. (2018), F2019 - model by Feng and Ritzwoller (2019), B2020 - model by Berg et al. (2020), Y2020 - model by Yang and Gao (2020), N2020 - model by Nayak et al. (2020), G2022 - model by Gama et al. (2022b). See Table 1 for more information about these velocity models.

141 also cover western Yukon, Canada (Figure 2b). In addition to the uneven coverage, these
 142 velocity model files are all in different model grids with different grid spacing and ranges.
 143 To facilitate quantitative comparisons, we interpolate all velocity models onto the same 3-D
 144 grids with grid sizes of 0.2 and 0.1 in longitudinal and latitudinal directions and 2 km in
 145 depth. The choice of grid spacing is based on a trade-off between efficiency and the precision
 146 of cluster boundaries. When interpolating, we keep the maximum resolvable depth of the
 147 original model (Table 1).

148 Most of the selected velocity models share similar large-scale features showing the
 149 change of velocity structures from the subduction margin to the south, through the
 150 continental interior, to the passive margin to the north (Figures 3 and 4). At the depth of 24
 151 km (Figure 3), most of the velocity models show low-velocity features below the Brooks
 152 Range in northern Alaska and higher velocities to the south in central Alaska (Figure 3a-b,
 153 d-e, and g-h). The models also consistently show relatively low velocities in western and
 154 eastern Alaska, and western Yukon (Canada). These velocity features can also be observed
 155 from M2018 (Figure 3c), though the overall velocity variation is much smaller than in other
 156 models. Y2020 doesn't cover the Brooks Range, though the increase in velocity from the
 157 southern margin to the interior is seen (Figure 3f). At the depth of 80 km (Figure 4), all
 158 velocity models show elongated high-velocity features parallel to the Aleutian volcano arc,
 159 corresponding to the subducting Pacific plate. However, these high-velocity features pos-

160 sess different velocities and are in different scales. The slab-like high-velocity features have
 161 lower amplitudes in model M2018 and are less well-resolved horizontally in G2022. The
 162 upper mantle velocities in central Alaska are generally lower than the surrounding areas,
 163 particularly those north of the Kobuk Fault Zone below the Brooks Range and further north.
 164 Relatively high upper mantle velocities are shown in northeastern Alaska and western Yukon
 165 (Canada) in all models.

Table 1. Seismic shear-wave velocity models synthesized in this study (ordered by publication date). For the N2020 model by Nayak et al. (2020), we only consider the AKAN2020 model that covers the entire study area.

Label	Data	Method	Depth (km)	Clusters	Reference
W2018	surface waves from ambient noise and teleseismic P-wave receiver functions	joint inversion	0 to 70	6	Ward and Lin (2018)
J2018	surface waves from ambient noise and teleseismic P-wave arrival times	joint inversion	0 to 800	6	Jiang et al. (2018)
M2018	surface waves from ambient noise and earthquakes and teleseismic P-wave receiver functions	joint inversion	0 to 200	5	Martin-Short et al. (2018)
F2019	surface waves from ambient noise and earthquakes	Bayesian inversion	0 to 200	6	Feng and Ritzwoller (2019)
B2020	surface waves from ambient noise and teleseismic P-wave receiver functions	joint inversion	0 to 144	6	Berg et al. (2020)
Y2020	surface waves from ambient noise	full-wave tomography	0 to 150	5	Yang and Gao (2020)
N2020	surface waves from ambient noise and body waves from earthquakes	travel-time inversion	-1 to 300	6	Nayak et al. (2020)
G2022	surface waves from ambient noise and teleseismic S-wave receiver functions	joint inversion	0 to 226	5	Gama et al. (2022b)

166 2.2 Crustal thickness models

167 Crustal thickness is a fundamental parameter in Earth science and is usually defined
 168 seismically as the depth to a nearly ubiquitous vertically-localized velocity increase, i.e., the
 169 Mohorovičić Discontinuity (Moho), somewhere within the upper 70 km of the Earth. Across
 170 Alaska, crustal thickness has been studied using seismic analyses for decades (e.g., Woppard
 171 et al., 1960; Fuis et al., 2008; Zhang et al., 2019). However, the recent TA deployment has
 172 greatly improved the coverage for estimating crustal thickness and allows for continuous
 173 analysis across the entire state. Here we compare crustal thickness estimates across Alaska

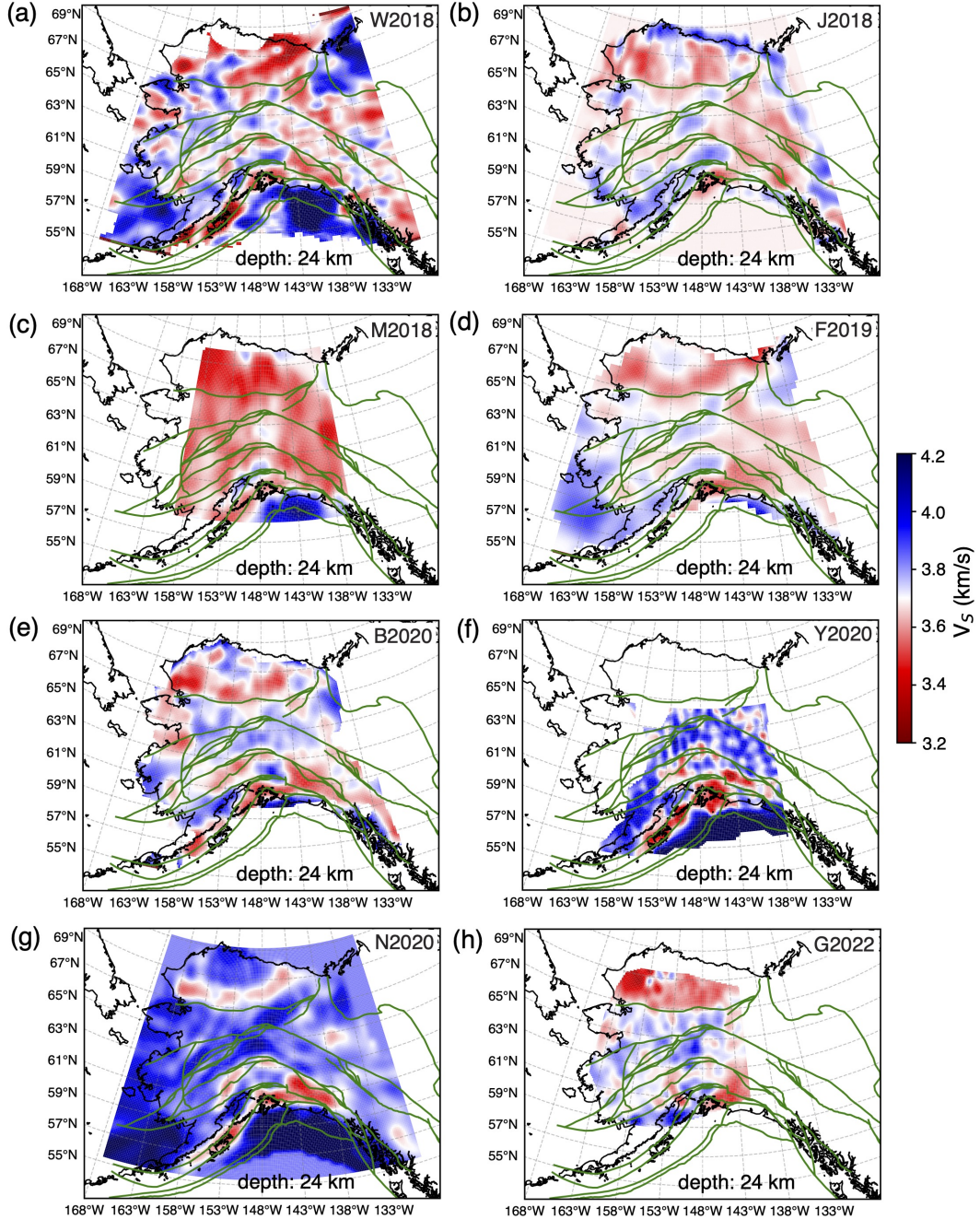


Figure 3. Examples of the synthesized shear-wave velocity models at the depth of 24 km. (a-h) Depth slices from models W2018 (Ward & Lin, 2018), J2018 (Jiang et al., 2018), M2018 (Martin-Short et al., 2018), F2019 (Feng & Ritzwoller, 2019), B2020 (Berg et al., 2020), Y2020 (Yang & Gao, 2020), N2020 (Nayak et al., 2020), and G2022 (Gama et al., 2022b). Major faults (thick green lines) are shown for reference. After interpolations onto 0.1 (longitudes) by 0.1 (latitudes) grids, we smooth all models laterally over five grids for plotting.

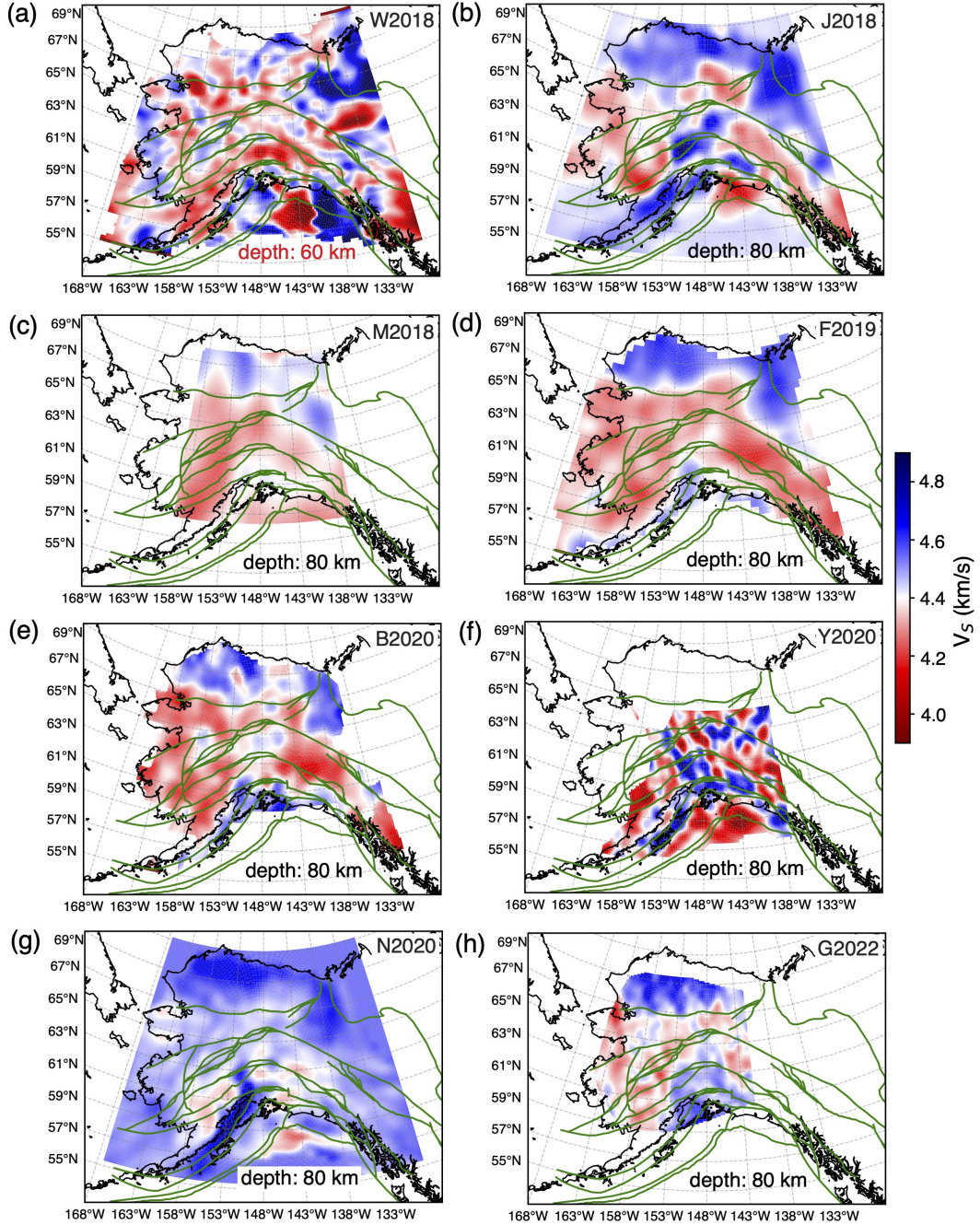


Figure 4. Same as Figure 3 but at the depths of 60 km for W2018 and 80 km for all other models. After interpolating onto 0.2 (longitudes) by 0.1 (latitudes) grids, we smooth all models laterally over five grids for plotting. See Figure S2 in the supplement for the velocity maps at the depth of 60 km for all models.

Table 2. Crustal thickness models synthesized in this study (ordered by the publication date). Mann et al. (2022) provide two sets of crustal thickness estimates: one for the continental crust beneath southeastern Alaska (Figure 6c), and the other for the thickness of the overriding crust above the subducting slab shallower than the intersection of the plate interface and continental Moho (Figure S1 in the supplement, with instructions to access the supplementary information in the **Availability Statement** section).

Model publication	Single-station estimates	Multi-station estimates
Ai et al. (2005)	X	-
Rossi et al. (2006)	X	-
Miller et al. (2018)	X	-
Zhang et al. (2019)	X	-
Haney et al. (2020)	-	X
Mann et al. (2022)	X	X
Gama et al. (2022a)	-	X

from various studies and combine a number of them to create an integrated crustal thickness dataset for the region.

We select and integrate the results from seven studies (Table 2) that explicitly measure crustal thickness across Alaska by determining the depth to a sharp velocity gradient, i.e., the Moho. The results from the selected studies can be split into two groups: single-station and multi-station estimates of crustal thicknesses (Table 2). The single-station estimates (Ai et al., 2005; Rossi et al., 2006; Miller et al., 2018; Zhang et al., 2019) all involve the analysis of teleseismic P-wave receiver functions, which are time series of converted S waves generated from passing teleseismic P waves (e.g., Langston, 1977). These studies yield one value of crustal thickness beneath each seismic station (e.g., Figure 5). The multi-station estimates yield maps of crustal thickness beneath and between nearby stations (e.g., Haney et al., 2020; Gama et al., 2021; Mann et al., 2022), providing overlapping crustal thickness constraints (Figure 6). The crustal thickness maps from both Mann et al. (2022) and Gama et al. (2022a) were generated from back-projecting receiver functions to depth through a velocity model. Mann et al. (2022) used teleseismic P-wave receiver functions, and Gama et al. (2022a) used teleseismic S-wave receiver functions. The map from Haney et al. (2020) was created using an inversion that solves for crustal thickness, as well as the shear velocity of the crust and an underlying mantle half-space, with an approximation based on the Dix equation to relate fundamental mode Rayleigh wave phase velocities to the velocity model.

In addition to the seven studies selected for comparison, other measures of crustal thickness in Alaska also exist. Among studies that solve for 3D velocity structure, those that jointly invert surface wave dispersion with P receiver functions (e.g., Martin-Short et al., 2018; Ward & Lin, 2018; Feng & Ritzwoller, 2019; Berg et al., 2020) or with S receiver functions (e.g., Gama et al., 2021, 2022b) typically provide sharper resolution of the depth of the Moho velocity gradient than other approaches. However, the studies in these groups that sample mainland Alaska are represented in the analysis of shear-wave velocity models in Section 2.1 and their crustal thickness results are not explicitly considered in this section. Additional estimates of crustal thickness based solely on receiver functions also exist (e.g., Veenstra et al., 2006; Rondenay et al., 2008, 2010; Kim et al., 2014; Brennan et al., 2011; Allam et al., 2017) but are not explicitly shown here, typically because the regions they

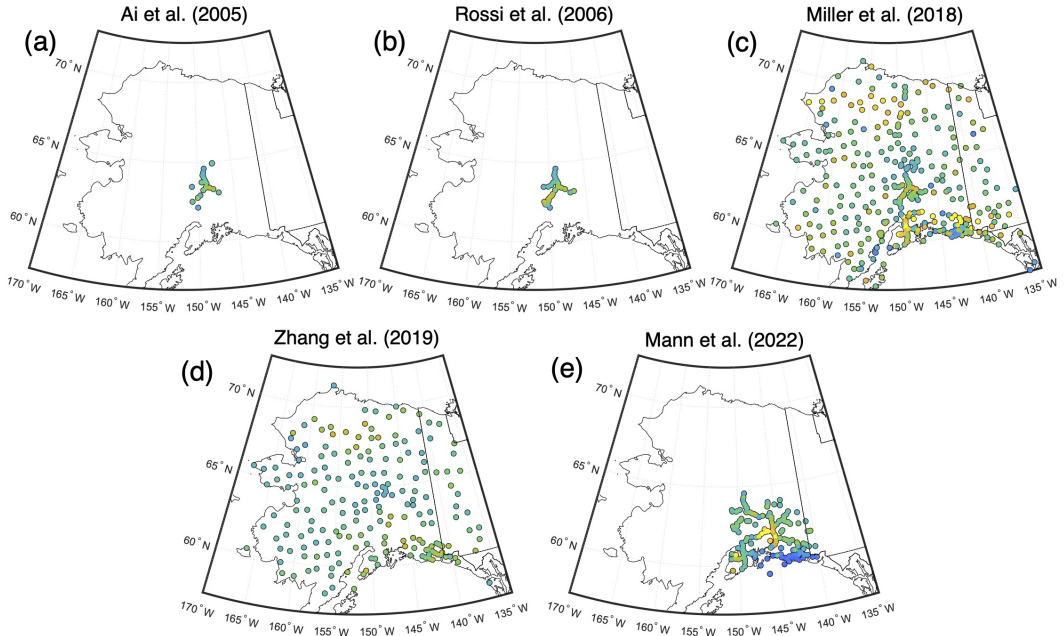


Figure 5. Single-station crustal thickness estimates from (a) Ai et al. (2005), (b) Rossi et al. (2006), (c) Miller et al. (2018), (d) Zhang et al. (2019), and (e) Mann et al. (2022).

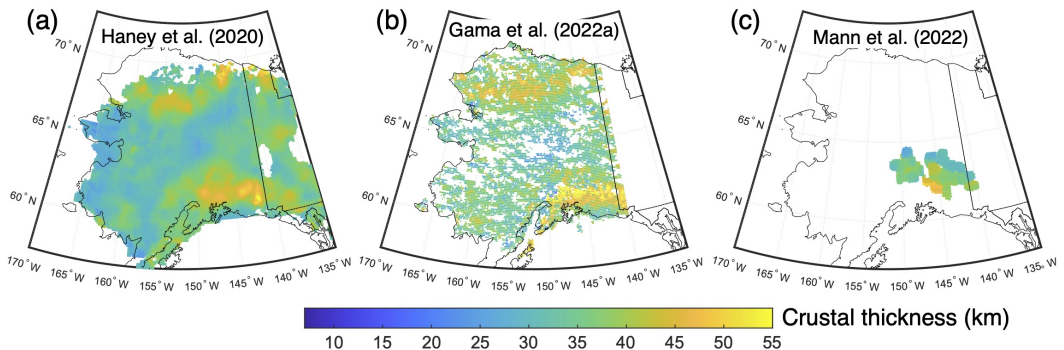


Figure 6. Multi-station continental crustal thickness estimates from (a) Haney et al. (2020), (b) Gama et al. (2022a), and (c) Mann et al. (2022).

sample are replicated in the studies in Table 2 and/or their crustal thickness values were not digitally available.

Among the selected studies (Table 2), the estimation of crustal thickness encounters complexity in the shallow part of the subduction zone, where the subducting crust is in contact with the overriding crust. In this case, there are typically multiple sharp velocity gradients (e.g., Bostock, 2013). Mann et al. (2022) mapped out the depth of the plate interface at depths <60 km (Figure S1 in the supplement, which is available through the Zenodo repository as described in **Availability Statement**). We use these values to determine the location of a line, referred to as the Plate Interface Extent (PIE) line, that represents where the plate interface intersects the base of the continental crust. For simplicity, we assume that this contact occurs at a depth of 40 km (Figure S1 in the supplement), although in reality, this contact depth varies. South of the PIE line, the continental crust is in contact with the subducting plate and multiple velocity gradients exist which obscure crustal

217 thickness estimates. Mann et al. (2022) directly accounted for the multiple crustal velocity
 218 gradients when measuring the plate interface depth, which is equivalent to the thickness of
 219 the overriding continental crust south of the PIE line (Figure S1 in the supplement).

220 Note, although we use the term plate interface extent (PIE), we emphasize that it is a
 221 crust-crust contact in that it refers to the separation of the top of the crust in the downgoing
 222 plate from the base of the crust in the overriding plate. If there is any mantle lithosphere
 223 present in the overriding plate, then the top of subducting crust would be in contact with
 224 the mantle lithosphere at the base of the overriding plate north of the PIE line.

225 3 Methods

226 To synthesize the two different types of models, i.e., the shear-wave velocity models
 227 and the crustal thickness models, we apply two categories of analyses. Considering lateral
 228 variations in the shear-wave velocity models, we use unsupervised K-means clustering of the
 229 1-D velocity profiles to objectively analyze the regionalization of the 3-D velocity structure.
 230 This is also a way to reduce the dimension of the velocity models for the synthesis and
 231 has been effective in tectonic regionalization of global seismic velocity models (e.g., Lekic
 232 & Romanowicz, 2011; Schaeffer & Lebedev, 2015). For the crustal thickness models, we
 233 focus on the statistical analysis of all models by averaging the crustal thickness estimates.
 234 In the following paragraphs, we describe the details of the procedures for comparing and
 235 synthesizing the selected seismic models.

236 3.1 K-means clustering of 1-D seismic velocity profiles

237 K-means clustering is commonly used to group data points based on their distances
 238 from the cluster centers. We use the *Tslearn* Python toolkit (Tavenard et al., 2020) for
 239 K-means clustering of time-series data to cluster the seismic velocity profiles (1-D depth
 240 profiles). The clustering operations are implemented as Python wrapper functions in the
 241 *SeisGo* toolbox (Yang et al., 2022a, 2022b). As described in Section 2.1, all velocity models
 242 are resampled onto the same 3-D grid with spacings of 0.2° in the longitudinal direction,
 243 0.1° in the latitudinal direction, and 2 km in the depth direction. The resampled velocity
 244 models are clustered through the following steps (see Section 4.1 for the description of key
 245 observations):

246 *Step 1: Determine the depth range for clustering.* The velocity models to be analyzed
 247 have different depth ranges. This step sets the depth range of interest. From Figures 3 and 4
 248 and Section 2.1, we observe varying velocity patterns from different velocity models, though
 249 they all show a lateral variation of velocities across Alaska and western Yukon (Canada).
 250 However, Figure 3 (as an example of crustal velocities) and Figure 4 (as an example of
 251 mantle lithosphere velocities) reveal different velocity features. Therefore, in this study, we
 252 divide the continental lithosphere into two depth ranges: 10-50 km and 40-120 km. We use
 253 the minimum depth of 10 km to account for the lack of resolution at shallower depths in
 254 some of the velocity models, such as J2018 (Jiang et al., 2018), M2018 (Martin-Short et
 255 al., 2018), and Y2020 (Yang & Gao, 2020). Considering the overall crustal thickness within
 256 the study area (Section 2.2 and Figures 5 and 6), we use the depth range of 10-50 km to
 257 represent the crust for clustering purposes. The depth of 120 km would include the total
 258 thickness of the upper plate lithosphere over most of the study area, with the exception of
 259 some of the thickest lithosphere in northern Alaska (Miller et al., 2018; Gama et al., 2021,
 260 2022b). However, in central Alaska, the lithosphere is much thinner (Gama et al., 2022a),
 261 and a maximum depth of 120 km would also include the asthenospheric mantle. Hence we
 262 use the depth range of 40-120 km for the mantle clustering analysis, to capture variations
 263 in the structure of the mantle lithosphere of the continental plate while avoiding too much
 264 dilution of the lithospheric structure by the asthenospheric mantle.

265 *Step 2: Choose the number of clusters for each velocity model.* Specifying the number
 266 of clusters is required to run K-means clustering. To account for the different coverage of
 267 each velocity model, we choose 6 clusters for models that cover all of Alaska and the western
 268 Yukon (Canada) area, including W2018, J2018, F2019, B2020, and N2020 models (Figure
 269 2b and Table 1). For models that only cover portions of the study area, including M2018,
 270 Y2020, and G2022, we choose 5 clusters (Figure 2b and Table 1). The clustering function in
 271 *SeisGo* (Yang et al., 2022a) has the option of automatically determining the optimal number
 272 of clusters. For models in Table 1, the automatically determined numbers of clusters range
 273 from 5 to 8, resulting in small-scale clusters in some cases while producing similar major
 274 clusters as the results using the pre-assigned number of clusters. Although the choice of the
 275 number of clusters is somewhat subjective, it does not change the overall conclusions of the
 276 analysis (Section 4).

277 *Step 3: Smooth the 3-D velocity model and build an ensemble of 1-D velocity profiles.*
 278 Due to the difference in data and methods, the selected velocity models may have different
 279 spatial resolutions. For instance, models W2018 (Ward & Lin, 2018) and Y2020 (Yang &
 280 Gao, 2020) show more small-scale features than other models (Figures 3 and 4). To focus on
 281 major velocity clustering patterns, we smooth all velocity models with a boxcar smoother
 282 across 5 grid points in both longitudinal and latitudinal directions but not in the depth
 283 direction. After smoothing the model, we build an ensemble of 1-D velocity profiles. The
 284 1-D velocity profile at each longitude-latitude grid can be treated as a time series. This step
 285 generalizes the seismic velocity clustering into the clustering of a time series dataset.

286 *Step 4: Conduct clustering of the ensemble of 1-D velocity profiles.* We use the Eu-
 287 clidean distance as the distance metric in clustering. The clustering results are shown in
 288 Figures 7 and 8 for the depths of 10-50 km and 40-120 km, respectively. The cluster labels
 289 are randomly assigned for each velocity model and are not directly comparable across dif-
 290 ferent models. The cluster centers and the standard deviations are shown in Figures S3 and
 291 S4 for the depths of 10-50 km and 40-120 km, respectively.

292 *Step 5: Detect cluster boundaries.* To compare the regionalization of the velocity struc-
 293 tures from different models, we detect the boundaries between clusters from the clustering
 294 images that are color-coded by the cluster labels (Figures 7 and 8). We compute the binary
 295 gradient around each resampled model grid or image pixel. The gradient is 0 if all four
 296 pixels have the same cluster label as the center pixel and 1 if there is at least one neighbor-
 297 ing pixel in a different cluster, which means the center pixel is at a cluster boundary. The
 298 detected cluster boundaries for each velocity model are shown as red pixels in Figures S5
 299 and S6 in the supplement for the clustering results at the depth of 10-50 km and 40-120 km,
 300 respectively.

301 *Step 6: Compute votes of cluster boundaries from all models.* To highlight the cluster
 302 boundaries that are shared by multiple velocity models, we stack all images of the cluster
 303 boundaries and compute the total times a model grid (or image pixel) is detected as a cluster
 304 boundary. This step produces a vote map showing the distribution of cluster boundaries
 305 with all velocity models (Figure 9a-b). A higher vote means more models detect the cluster
 306 boundaries. From the vote maps of detected cluster boundaries, we identify the major
 307 velocity domains as outlined by cluster boundaries with ≥ 3 votes and extract the average
 308 velocity profiles within the domains (Figure 10). To minimize the bias, we pick cluster
 309 boundary lineaments and velocity domains solely based on the cluster boundary vote maps
 310 without referencing the fault lines and tectonic terranes.

311 3.2 Averaging of crustal thickness estimates

312 We compute the average and standard deviation of crustal thicknesses separately for the
 313 compiled single- and multi-station results (Table 2) within grid nodes spaced 0.5° (longitude)
 314 by 0.25° (latitude) apart (Figure 11 and S9 in the supplement). We choose this grid spacing
 315 based on the general station spacing (50-80 km) and the resolution of the final model.

316 For the multi-station crustal thickness map (Figure 11b), we use the plate interface depth
 317 from Mann et al. (2022) (Figure S1 in the supplement) as the thickness of the overriding
 318 continental crust south of the PIE line, avoiding complexity due to the presence of both the
 319 upper-plate crust and the subducting crust. North of the PIE line, the crustal thickness
 320 simply corresponds to the mean Moho depth estimate, which is the base of the continental
 321 crust.

322 4 Results

323 4.1 Cluster maps of seismic velocity profiles

324 The clustering of crustal velocities (10-50 km) highlights the lateral variations correlated
 325 with major faults (Figure 7). In the cluster map of model W2018 (Figure 7a), the southern
 326 Alaska region south of the Denali Fault System is dominated by cluster 2. The region north
 327 of the Kobuk Fault Zone shows three clusters (2, 3, and 5). The western Yukon region is
 328 characterized by clusters 1, 2, and 5. The rest of the study area, mostly between the Kobuk
 329 Fault Zone and the Denali Fault System, is characterized by cluster 5. The clustering
 330 patterns from south to north across Alaska separated by the Denali Fault System and the
 331 Kobuk Fault Zone can also be observed from other models (Figure 7b-7e and 7g-7h). The
 332 cluster map of Y2020 (Figure 7f) also reveals the contrast in velocity patterns across the
 333 Denali Fault System, although lacks coverage in northern Alaska. Models J2018, F2019,
 334 B2020, N2020, and G2022 also show the variation of velocity patterns/clusters from west
 335 to east across Alaska, as well as across the Porcupine Shear Zone in northeastern Alaska
 336 (Figure 7d, 7e, and 7g-7h). In addition, the Pacific Plate in the northern Gulf of Alaska is
 337 characterized as separated clusters in models ML2018 (clusters 1 and 6), M2018 (cluster 4),
 338 Y2020 (cluster 3), and N2020 (clusters 3 and 6) with prominently higher velocities than the
 339 onshore area (Figure S3 in the supplement).

340 The velocity clustering patterns in the mantle lithosphere (40-120 km) show correlations
 341 with both major faults and the subduction zone along the southern margin of Alaska (Figure
 342 8). We observe separated clusters across the Kobuk Fault Zone (models W2018, J2018,
 343 F2019, B2020, N2020, and G2022 in Figure 8a-b, d-e, and g-h), the Porcupine Shear Zone
 344 (models W2018, J2018, M2018, F2019, B2020, and N2020 in Figure 8a-e and g), the Kaltag
 345 Fault (models F2019 and N2020 in Figure 8d and g), the Denali Fault System from all
 346 models, and the Tintina Fault (models W2018, J2018, M2018, F2019, B2020, and N2020
 347 in Figure 8a-e and g). However, some of the cluster boundaries only follow part of the
 348 fault lines. In southwestern Alaska, we observe elongated cluster regions sub-parallel to
 349 the subduction margin in multiple cluster maps, including the results from models J2018
 350 (cluster 4), M2018 (cluster 4), F2019 (clusters 4 and 5), B2020 (cluster 3), Y2020 (cluster
 351 5), N2020 (clusters 3 and 5), and G2022 (cluster 3). Most of these margin-parallel zones
 352 are located west of approximately 150°W in longitude. To the east, some models reveal a
 353 different cluster parallel to the margin, such as cluster 3 in J2018, cluster 1 in M2018, cluster
 354 2 in B2020, cluster 4 in N2020, and cluster 4 in G2022. In Y2020, cluster 5 spans across the
 355 majority of the margin with a gap at around 145°W in longitude (Figure 8f). It is worth
 356 noting that parts of these margin-parallel cluster zones overlap with the crustal clusters to
 357 the south of the Denali Fault System (Figure 8d-e and g-h). Compared to the crustal cluster
 358 maps in Figure 7, the mantle cluster maps contain more small-scale variability, particularly
 359 those from models W2018 (Figure 8a), J2018 (Figure 8b), and G2022 (Figure 8h).

360 4.2 Major velocity domains revealed by cluster boundaries

361 The vote maps of the velocity model cluster boundaries reveal major structural domains
 362 shared across multiple velocity models. The cluster boundaries from individual models show
 363 different patterns from model to model (Figures S5-S6 in the supplement). However, by
 364 combining the detection of cluster boundaries from all models, the vote maps in Figure 9
 365 highlight the cluster boundaries that are shared by multiple velocity models, shown as darker

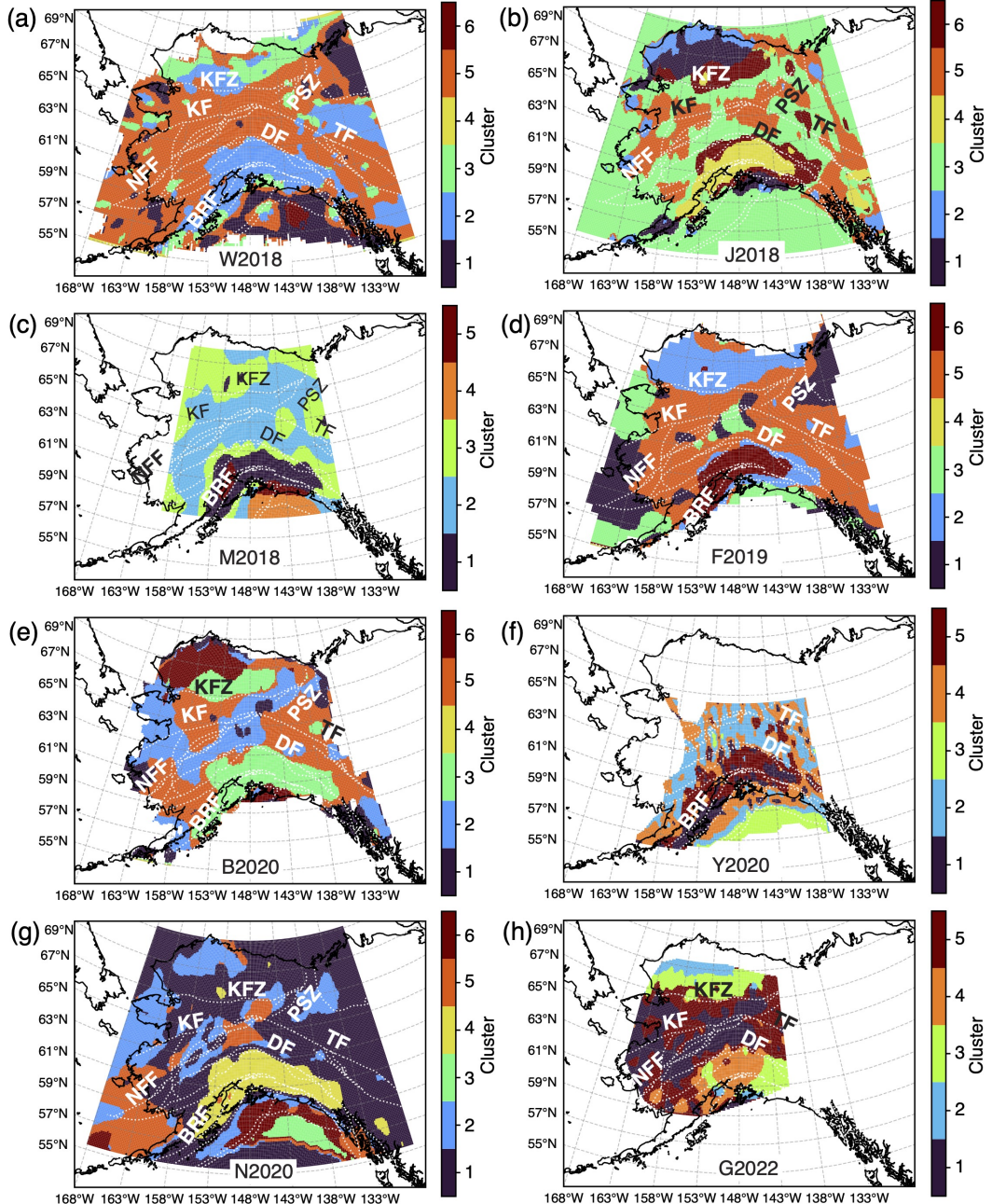


Figure 7. Clustering of velocity profiles between 10-50 km depths. The randomly-assigned cluster numbers are color-coded for each velocity model. The same cluster numbers for different velocity models may correspond to different velocity profiles. (a-h) Clustering results for models W2018 (Ward & Lin, 2018), J2018 (Jiang et al., 2018), M2018 (Martin-Short et al., 2018), F2019 (Feng & Ritzwoller, 2019), B2020 (Berg et al., 2020), Y2020 (Yang & Gao, 2020), N2020 (Nayak et al., 2020), and G2022 (Gama et al., 2022b). The dotted white lines are the fault lines as in Figure 1b. Labels of major faults: KFZ - Kobuk Fault Zone, KF - Kaltag Fault, PSZ - Porcupine Shear Zone, NFF - Nixon Fork-Iditarod Fault, TF - Tintina Fault, DF - Denali Fault System, BRF - Border Range Fault.

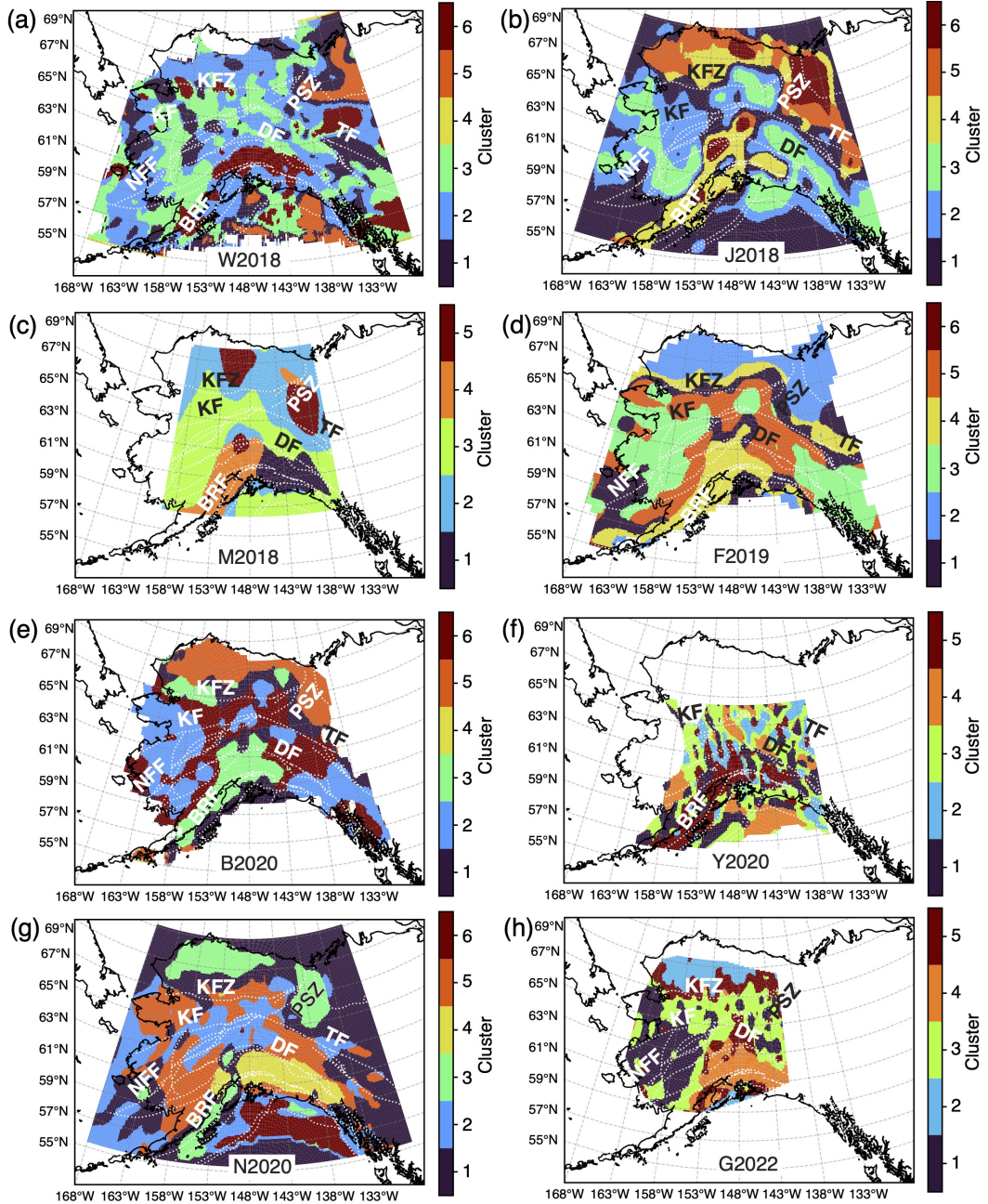


Figure 8. Same as Figure 7 but for velocity profiles at the depths of 40-120 km. The randomly-assigned cluster numbers are color-coded for each velocity model. The dotted white lines are the fault lines as in Figure 1b. See Figure 7 for the labels of major faults.

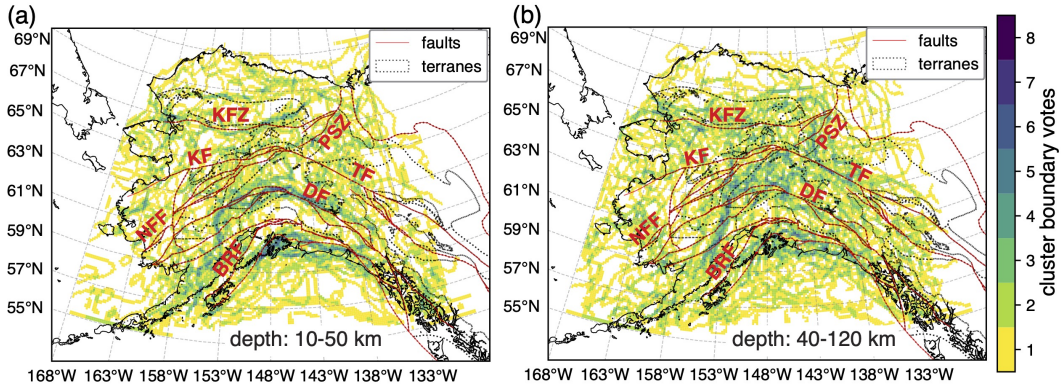


Figure 9. Detected cluster boundaries from all velocity models. (a-b) Cluster edge vote counts for the depths of 10-50 km and 40-120 km, respectively. Major faults (red solid lines) and terrane outlines (gray dotted lines) are shown for reference. See Figure 7 for the labels of major faults.

366 colors. Figure 10 shows the cluster boundary vote maps (blue pixels) with ≥ 3 votes. Due
 367 to the difference in spatial coverage of different models (Figure 2b), southern and central
 368 Alaska are sampled by all eight models while other areas are sampled by at least five models.
 369 The threshold of 3 strikes a balance between highlighting major velocity domains shared by
 370 multiple models and having enough connectivity among pixels of the cluster boundaries to
 371 show major lineaments.

372 We identify 6 major velocity domains in the crust (C1-C6) and mantle lithosphere (M1-
 373 M6) defined by the cluster boundary lineaments (Figure 10a-b). These velocity domains
 374 outline major areas without noticeable lineaments of cluster boundary votes. Domain C1
 375 overlaps with most of the area north of the Brooks Range in northern Alaska. C2 is mostly
 376 along the Brooks Range. Domains C3-C5 are located in the interior and western Alaska
 377 between the Brooks Range to the north and the Alaska Range to the south. C6 is located
 378 in southern Alaska covering the Alaska Range and the region to the south. For the mantle
 379 lithosphere, domain M1 spans across the Brooks Range and the North Slope area to the
 380 north. M2 occupies most of western Alaska and part of the interior. M3 is located to the
 381 southeast of M1 and to the east of M2. To the south, it is adjacent to domain M4, which
 382 is characterized by a group of small-scale cluster boundaries. To the south of M4, domains
 383 M5 and M6 are separated by a northwest-southeast trending cluster boundary lineament
 384 approximately along the Denali Fault System.

385 4.3 Velocity profiles within major domains

386 The average velocity profiles within the crustal velocity domains show similar overall
 387 patterns of increasing velocities with depth (Figure 10c). The velocities within domain C1
 388 are lower than those within domains C3-C5 at the depths of < 25 km. The velocities within
 389 domain C6 are lower than those for C3-C5 below the depth of 25 km. Domain C2 has
 390 velocities that are typically 0.2-0.3 km/s lower than other domains. The average shear-wave
 391 velocities reach 4.2 km/s at the depth of 35 ± 2 km within domains C1 and C3-C5, 40 ± 1 km
 392 within domain C2, and 45-46 km within domain C6. Domain C6 south of the Denali Fault
 393 System indicates the smallest velocity change over the entire depth range from 3.5 km/s
 394 to 4.25 km/s. In contrast, domain C1 shows the largest velocity range from 3.25 km/s to
 395 4.5 km/s. However, there are notable variations across different velocity models for these
 396 domains (Figure S7 in the supplement).

397 The mantle velocity domains show distinctly different average velocity profiles, partic-
 398 ularly below the depth of 45 km (Figure 10d). Domain M1 has the overall highest velocity
 399 of 4.5-4.6 km/s below the depth of 50 km. Domains M2 and M6 both show a low-velocity
 400 zone at depths of about 60-120 km with a minimum velocity of 4.3 km/s at the depth of
 401 about 100 km. Domain M3 also contains a decrease in velocity at a similar depth range as
 402 M2 and M6 but with a lower amplitude. Below the depth of 45 km, domain M4 has the
 403 smallest overall velocity variation with an almost constant velocity of 4.4 km/s. Domain
 404 M5 shows the largest velocity variation of 0.5 km/s from 4 km/s to 4.5 km/s. The velocity
 405 profile for domain M5 is also monotonically increasing although the rate of increase becomes
 406 small below the depth of 90 km. Similar to the crustal domains, while we focus more on

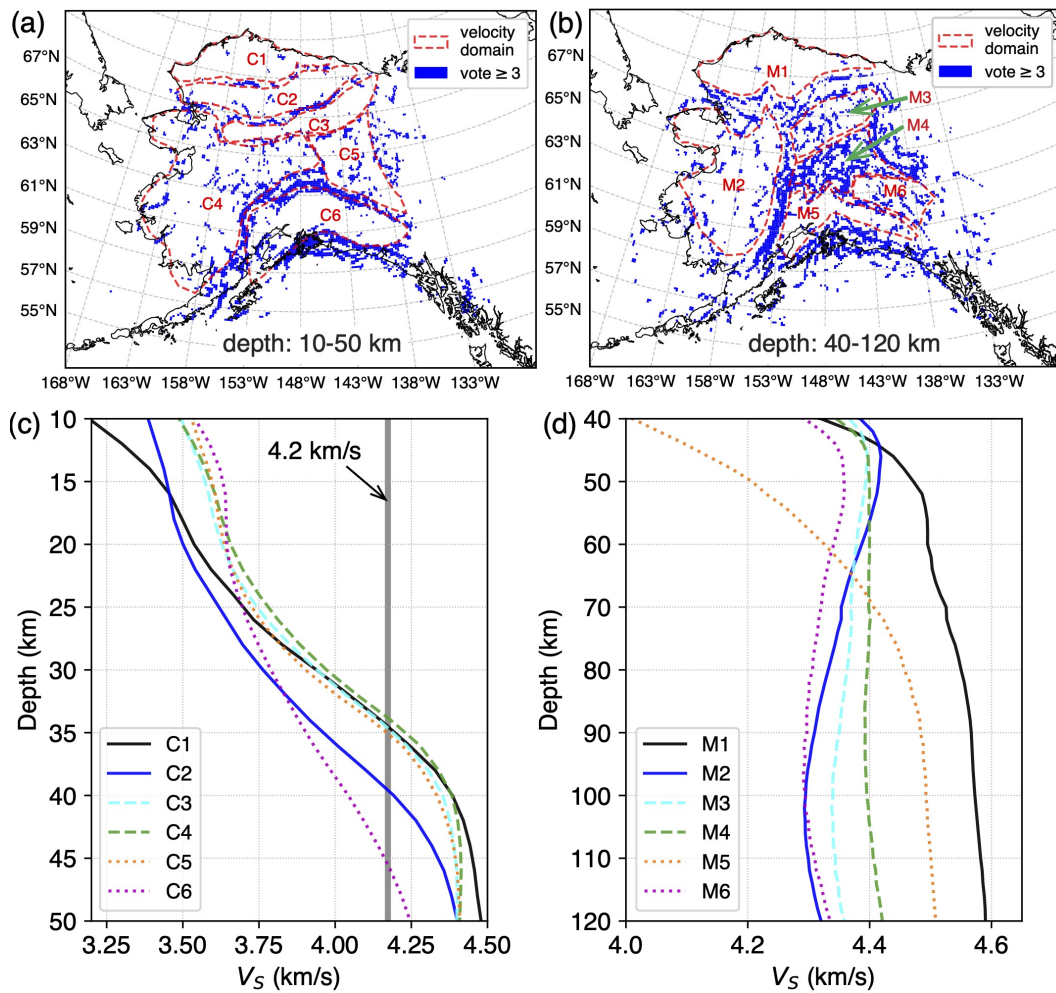


Figure 10. Major seismic velocity domains and the average velocity profiles. (a-b) Identified major velocity domains (alphanumeric labels C1-C6 and M1-M6 within the red dashed outlines) with ≥ 3 votes (blue pixels) for the depths of (a) 10-50 km and (b) 40-120 km. (c-d) Velocity profiles within each velocity domain averaged across all models at the depths of (c) 10-50 km and (d) 40-120 km. The thick gray vertical line in (c) is the $V_S=4.2$ km/s line as the minimum velocity of melt-free ultramafic materials (e.g., Delph et al., 2021), which is used here as a proxy to denote the velocity at the bottom of the crust. See Figures S7-S8 in the supplement for the velocity profiles from different velocity models for each velocity domain.

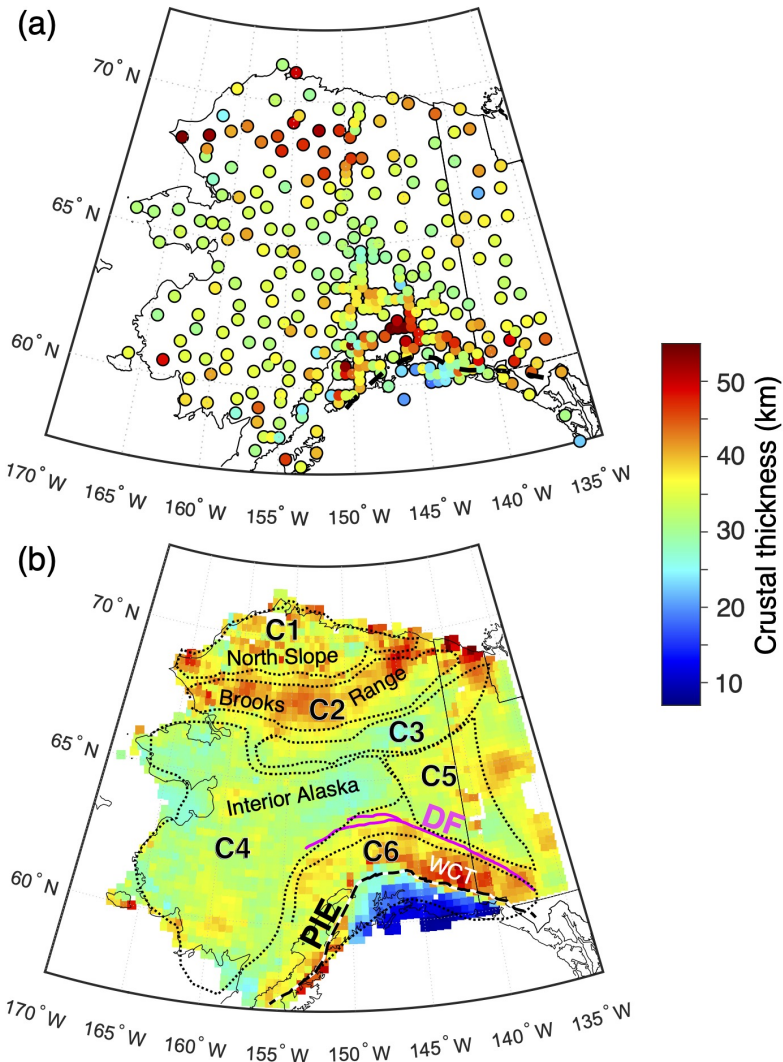


Figure 11. Average crustal thicknesses from multiple models. (a) Average of crustal thicknesses for single-station estimates. (b) Average of multi-station crustal thicknesses within each 0.5° (longitude) by 0.25° (latitude) bin. The dotted lines are outlines of the crustal seismic velocity domains as in Figure 10a, defined based on velocity clustering results. To the south of the Plate Interface Extent (PIE) line, the map is showing the depth to the top of the subducting plate. DF - Denali Fault System, WCT - Wrangellia Composite Terrane.

407 the average profiles, it is worth noting that the velocity profiles for the mantle domains also
408 vary significantly across different models (Figure S8 in the supplement).

409 4.4 Average crustal thickness

410 The average crustal thicknesses are shown in Figure 11a for the single-station averages
411 and Figure 11b for the multi-station averages. The standard deviations are much higher
412 south of the PIE line than to its north (Figure S9b), reflecting larger discrepancies among
413 different studies in this region. This may result from the presence of multiple positive
414 velocity gradients within both the upper plate and the shallowly-dipping downgoing plate
415 in this region. Different studies may have selected different interfaces below a given station

in this case. After accounting for the plate interface, the mean crustal thickness map from multi-station estimates (Figure 11b) shows a good agreement overall with the average of the single-station estimates (Figure 11a). However, in some locations, the average crustal thicknesses differ by more than 15 km. Some of these discrepancies are significant, in the sense that the standard deviations for the mean crustal thicknesses do not overlap. The Moho depth standard deviations north of the PIE line are typically lower for the multi-station crustal models (Figure S9d) than for the single-station results (Figure S9b), indicating more consistency across the individual multi-station crustal thickness models. Given this greater consistency and the more continuous lateral coverage provided by the multi-station models, we recommend the crustal thicknesses in Figure 11b as a reference model for continental Alaska.

We observe four notable crustal thickness patterns as revealed by the preferred reference model for Alaska (Figure 11b). 1) The crust across much of interior Alaska, approximately between the Alaska Range to the south and the Brooks Range to the north, is about 25–35 km thick, similar to the observations from previous studies (e.g., Woppard et al., 1960; Clarke & Silver, 1991; Searcy et al., 1996; Ai et al., 2005; Rossi et al., 2006; Veenstra et al., 2006; Brennan et al., 2011; Allam et al., 2017; Miller et al., 2018; Martin-Short et al., 2018; Zhang et al., 2019; Haney et al., 2020; Gama et al., 2021, 2022a, 2022b; Mann et al., 2022). 2) The Brooks Range in northern Alaska has a 40–50 km thick crust, which is similar to previous estimates (e.g., Woppard et al., 1960; Fuis et al., 1995, 1997; Searcy et al., 1996; Miller et al., 2018; Zhang et al., 2019; Haney et al., 2020; Gama et al., 2021, 2022b, 2022a). 3) The Wrangellia composite terrane in the south has a 35–55 km thick crust, as in previous studies (e.g., Fuis & Plafker, 1991; Haney et al., 2020; Gama et al., 2022a, 2022b). The crustal thickness of the Wrangellia composite terrane south of the Denali Fault System increases from 35 km to >50 km from west to east. 4) A laterally sharp northward decrease in crustal thickness of about 10 km exists across the Denali Fault System, similar to the observations in previous studies (e.g., Rossi et al., 2006; Veenstra et al., 2006; Brennan et al., 2011; Ward & Lin, 2018; Allam et al., 2017; Miller et al., 2018; Martin-Short et al., 2018; Haney et al., 2020; Mann et al., 2022; Gama et al., 2022a, 2022b).

5 Discussion

The patterns highlighted in Section 4 reveal major domains in terms of the integrated shear-wave velocity models (Figures 9 and 10) and crustal thicknesses (Figure 11). In this section, we place these results in the context of Alaskan tectonics and the evolution of the continental lithosphere.

5.1 Influence of crustal thickness on velocity clustering

The crustal velocity domains defined by the clustering of velocity profiles demonstrate a strong correlation with the crustal thickness patterns (Figure 11b). To examine the quantitative relationship between crustal thickness patterns and the velocity domains, we extract the average crustal thickness in each domain for both the crustal and mantle velocity domains (Figure 12). We also compare the crustal thickness within the crustal velocity domains with the depth along the average velocity profiles at a shear-wave velocity of 4.2 km/s, which is the minimum shear-wave velocity of melt-free ultramafic materials (e.g., Delph et al., 2021). Figure 12a shows that the depth to $V_S=4.2$ km/s in domains C1–C5 is roughly similar to the average crustal thickness, following the reference line (slope=1). The crustal thickness for domain C6 is about 36 ± 7.5 km, with a large error bar (Figure 12a–b). This may result from the fact that domain C6 spans across the PIE line, south of which the values are the depth to the plate interface, which dips to the north and thus varies significantly (Figure 11b). The same explanation is applicable to the crustal thickness for domain M5, which also has a large error bar (Figure 12c).

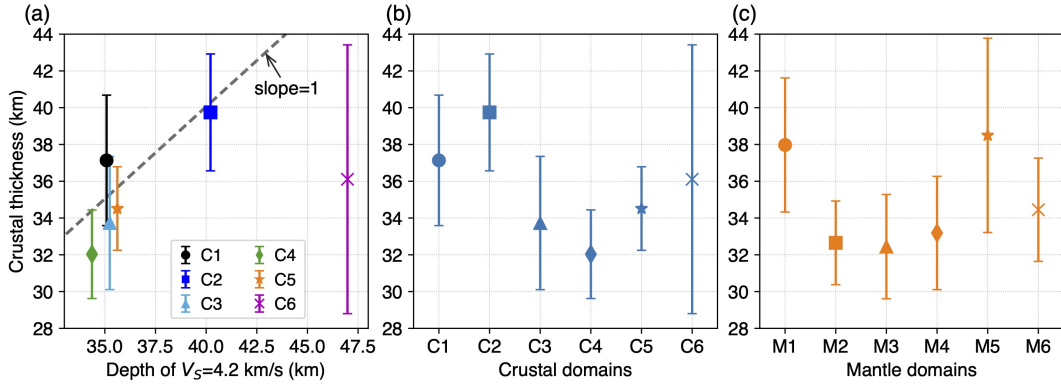


Figure 12. Crustal thicknesses within the crustal (C1-C6) and mantle (M1-M6) velocity domains using the multi-station average model in Figure 11b. (a) Comparison of crustal thicknesses within the crustal velocity domains (C1-C6) and the depths to the $V_s=4.2$ km/s on the average velocity profiles in Figure 10c. The error bar shows the standard deviation of the crustal thicknesses within each domain. The dashed line, with a slope of 1, is plotted for reference. (b) Crustal thicknesses within the crustal velocity domains (C1-C6) as defined by clustering of the velocities at the depths of 10-50 km. (c) Crustal thicknesses within the mantle velocity domains (M1-M6) as defined by clustering of the velocities at the depths of 40-120 km.

The clustering analysis in this study focuses on the holistic patterns of velocity profiles and, thus, crustal thickness information is implicitly considered. Crustal thickness clearly plays a role in defining the crustal domains. For example, domains C1 and C2 have thicker crusts, relative to C3, C4, and C5, and the uncertainties for C2 and C4 do not overlap (Figure 12b). However, the difference in the internal velocity structure of the crust is also significant. For example, C1 and C2 have mean crustal thicknesses that differ by less than 3 km (Figure 12b), but these domains have contrasting velocity profiles, with C2 containing lower velocities in the crust below 20 km depth (Figure 10c). On the other hand, domains C3, C4, and C5 in the central latitudes of Alaska have similar crustal thicknesses and similar internal velocity structures. These cases highlight the fact that the average velocity profiles from all models (Figure 10c) oversimplify some aspects of the crustal structure. The boundaries of C3, C4, and C5 were defined using the velocity profile clusters from at least three individual studies (Figure 10a), indicating that contrasts in velocity profiles between these domains do exist in some individual models. This result is backed up by the comparison of the cluster profiles for individual models (Figure S7), which indicates more complicated internal velocity heterogeneity. However, when the profiles of all models are averaged (Figure 10c), some of these differences are less evident. Average crustal thicknesses are also shown for the mantle domains (Figure 12c). With velocities from depths of 40-120 km, the mantle velocity clustering should be much less influenced by the variation of crustal thicknesses, which are <40 km in most of the study area (Figure 11b).

485 5.2 Mantle heterogeneity of the seismic domains

The mantle seismic structural domains possess distinctly different velocity structures, associated with varying lithospheric thicknesses, and in some cases with the influence of the subducting lithosphere. Comparison of the average velocity profiles in these domains indicates that mantle structure in Alaska can be divided into three broad domains: northernmost Alaska (M1), mantle containing subducting lithosphere in the south (M5), and everything in between (M2-M4 and M6).

492 Domain M1, in northernmost Alaska, is in a passive continental margin setting (e.g.,
 493 Colpron et al., 2007; Müller et al., 2019), and its outline approximately matches the North
 494 Slope subterrane of the Arctic Alaska terrane (AAns in Figure 13a; Plafker & Berg, 1994;
 495 Colpron et al., 2007). The M1 domain is distinguished by the thickest and highest velocity
 496 mantle lithosphere that is found in Alaska (Figure 10d), matching the conclusions of a wide
 497 range of studies (O'Driscoll & Miller, 2015; Martin-Short et al., 2018; Jiang et al., 2018; Feng
 498 & Ritzwoller, 2019; Berg et al., 2020; Gama et al., 2021, 2022a, 2022b). Heat flow is low
 499 relative to the rest of Alaska over much of the M1 domain, consistent with the low vertical
 500 thermal gradient in a thick mantle lithosphere (Batir et al., 2016). However, intriguingly,
 501 heat flow appears to increase in the northernmost tip of M1 (Batir et al., 2016). The M1
 502 domain is also largely devoid of seismicity (Ruppert & West, 2020), suggesting little ongoing
 503 internal deformation. Most of the M1 domain lies beneath the thick crust of the C1 crustal
 504 velocity domain, but it is bordered by the thick and low-velocity crust of the C2 domain
 505 (Figures 10 and 12b), which largely corresponds to the Hammond-Coldfoot subterrane of
 506 the Arctic Alaska terrane (AAh in Figure 13a) and the moderately high topography of the
 507 Brooks Range. Overall, these observations are consistent with geologic information that the
 508 M1 domain/North Slope Arctic Alaska terrane represents an anomalous continental terrane
 509 (Hubbard et al., 1987; Plafker & Berg, 1994; Colpron et al., 2007; Strauss et al., 2013) that
 510 experienced crustal shortening at its southern margin during its accretion. However, the
 511 new information provided by the analyses of EarthScope TA data clearly shows that the
 512 mantle lithosphere of this terrane is as distinctive as its crust, based on its large thickness,
 513 high velocities, and apparently low temperatures.

514 The overriding lithosphere over most of the rest of Alaska is relatively thin. Domains
 515 M2-4 and M6 show local minimum velocities at depths of 90-110 km, consistent with litho-
 516 sphere that ends above this depth (e.g., Martin-Short et al., 2018; Gama et al., 2022a, 2022b)
 517 (Figure 10d). The decrease of velocity for M4 within this depth range (90-110 km) is subtle
 518 but visible. This thinner lithosphere with an asthenospheric low-velocity layer is consistent
 519 with the higher heat flow observed in these domains (Batir et al., 2016). The lowest average
 520 asthenospheric velocities are observed in domains M2 and M6. M2 spans across the back-arc
 521 mantle of the main Alaska subduction zone. It reaches all the way to the Seward Peninsula
 522 where magmatic centers with decompression melting compositions occur (e.g., Mukasa et
 523 al., 2007). Domain M6, which also manifests the lowest average mantle lithospheric veloc-
 524 ities, is located to the northeast of the Wrangell Volcanic Field. It may also reflect melting
 525 in the back-arc mantle to the northeast of the Wrangell slab, characterized by the dipping
 526 seismicity and slab-alike high velocities (Yang & Gao, 2020; Daly et al., 2021; Mann et al.,
 527 2022). The lower velocities could be explained by the mobile back-arc tectonics (Hyndman
 528 et al., 2005) or the toroidal return flow around the eastern Alaska slab edge (Jadamec &
 529 Billen, 2010, 2012). Domain M4 spans across the North America basinal strata and the
 530 Yukon-Tanana terrane (Figure 13b) with a nearly constant average velocity of 4.4 km/s in
 531 the mantle lithosphere (Figure 10d). The abundance of velocity cluster boundaries in M4
 532 without clear lineaments (Figure 10b) suggests a highly heterogeneous mantle lithosphere
 533 in this region with strong lateral variations. M4 also overlaps with the northern corner of
 534 the shallowly subducting Yakutat Microplate (Figure 14; Hayes et al., 2018; Finzel, Flesch,
 535 Ridgway, Holt, & Ghosh, 2015; G. L. Pavlis et al., 2019), where a high-velocity body-wave
 536 anomaly is imaged (Figure 14). Additionally, M4 is located at the frontier of the Tintina
 537 Fault intersecting with the west-southwest to east-northeast trending Kaltag Fault (e.g.,
 538 Gabrielse et al., 2006; Audet et al., 2019; Esteve et al., 2020). Therefore, the strong lateral
 539 heterogeneity in M4 likely reflects a complex and highly deformed mantle lithosphere related
 540 to Yakutat Microplate subduction and its impact on upper plate deformation.

541 In contrast to the other mantle domains, M5, which lies within the footprint of the
 542 subducting lithosphere, does not on average show evidence of a well-developed layer of high-
 543 velocity mantle lithosphere (Figures 10d and 14). Rather, velocities remain relatively low
 544 above the depth of about 55 km (Figure 10d), likely representing the vertical juxtaposition
 545 of the overriding crust and that of the subducting plate, where the latter largely comprises a

546 thick Yakutat oceanic plateau (e.g., G. L. Pavlis et al., 2019; Chuang et al., 2017; Rondenay
 547 et al., 2010). The continued velocity increase likely represents the transition to the mantle
 548 of the subducting plate, which dominates the average velocity profile down to depths of 120
 549 km (Figure 10d).

550 5.3 Correlation of seismic domains with tectonic features

551 Many of the most prominent boundaries delineated by the clustering analysis of the
 552 velocity models strike approximately parallel to the trends of the tectonic terranes and major
 553 faults in Alaska (Figure 13). In southern Alaska, some of these trends are approximately
 554 east-west but concave to the south, parallel to the active convergent margin (e.g. domains
 555 C6 and M5). In northern Alaska, some structural trends are concave to the north (e.g.
 556 C1-C3), reflecting more ancient accretionary tectonic terranes.

557 The velocity model clustering and crustal thickness analyses indicate that the Denali
 558 Fault System, the Kobuk Fault Zone, and potentially the Porcupine Shear Zone represent
 559 lithospheric-scale boundaries that separate regions with distinct seismic structures. The
 560 dextral strike-slip Denali Fault System in southern Alaska has long been the target of geo-
 561 physical studies. With a well-documented 10-km northward thinning of the crust across the
 562 Denali Fault System and/or Hines Creek Fault (Figure 11b; Rossi et al., 2006; Veenstra et
 563 al., 2006; Brennan et al., 2011; Ward & Lin, 2018; Allam et al., 2017; Miller et al., 2018;
 564 Martin-Short et al., 2018; Haney et al., 2020; Mann et al., 2022; Gama et al., 2022a, 2022b),
 565 the overall Denali Fault System acts as a major crustal boundary that separates the Alaska
 566 Range and the Wrangellia composite terrane to the south and the North American affinity
 567 terranes in the interior of Alaska to the north (W. Nokleberg et al., 2013; Benowitz et
 568 al., 2022). High-resolution finite-element models of Alaska that incorporated a Denali fault
 569 lithospheric shear zone (Jadamec et al., 2013; Haynie & Jadamec, 2017) found a better fit
 570 to surface motion and regions of exhumation and subsidence in south-central Alaska than
 571 models that did not include a Denali fault shear zone (Jadamec & Billen, 2010, 2012). This
 572 suggests that the Denali Fault System may also represent a mantle structural boundary
 573 (Jadamec et al., 2013; O'Driscoll & Miller, 2015; Haynie & Jadamec, 2017). Recent work
 574 by Gama et al. (2022b) found a northward increase in total lithospheric thickness across the
 575 Denali Fault System, which in many places is accompanied by an increase in the shear-wave
 576 velocity of the mantle lithosphere (Gama et al., 2022b). The velocity clustering analysis in
 577 this study suggests that the Denali Fault System represents a major structural boundary in
 578 both the crust and mantle (Figure 13). In the crust, the Denali Fault System aligns with the
 579 northern margin of domain C6, and in the mantle, it lies at the southern boundary of domains
 580 M4 and M6, where they transition to domain M5. The southern boundary of the M4
 581 domain does not reach the western end of the Denali Fault System (Figure 13b). Instead, it
 582 terminates at the boundary that marks the eastern edge of the M2 domain corresponding to
 583 the edge of the high-velocity subducting lithosphere (Figure 14). However, this relationship
 584 suggests that the cluster analysis in the 40–120 km depth range might be the manifestation
 585 of the signature of the subducting oceanic lithosphere. It does not mean that the mantle
 586 signature of the Denali Fault System in the overriding plate necessarily ends here (Gama et
 587 al., 2022b).

588 The east-west trending Kobuk Fault Zone to the south of the Brooks Range in northern
 589 Alaska is today the site of low-rate dextral strike-slip motion (Elliott & Freymueller, 2020)
 590 with a mix of faulting styles developed over time (Avé Lallement et al., 1998). However,
 591 it has also been proposed as the ancient collisional boundary between the North Alaska
 592 Microplate to the north (including the North Slope and Hammond-Coldfoot subterranea)
 593 and the volcanic arc and other terranes to the south (Hubbard et al., 1987). The crustal
 594 thickness increases from 34 ± 3 km (C3) to 40 ± 3 km from south to north across the Kobuk
 595 Fault Zone (Figures 11b and 12b; Woppard et al., 1960; Clarke & Silver, 1991; Fuis et al.,
 596 1995, 1997; Searcy et al., 1996; Veenstra et al., 2006; Brennan et al., 2011; Allam et al.,
 597 2017; Miller et al., 2018; Zhang et al., 2019; Haney et al., 2020; Gama et al., 2021, 2022b,

598 2022a). As described in Section 5.2, the velocity clustering results indicate the Kobuk
 599 Fault Zone lies at the boundary of major velocity domains, including the C2-C3, and M1-
 600 M3 transitions (Figures 10a-b and 13). This observation is consistent with the view that
 601 lithospheric structural gradients help to localize deformation on this fault system.

602 To the southeast of the Brooks Range, the southwest-northeast trending Porcupine
 603 Shear Zone, with evidence of sinistral movement (von Gosen et al., 2019), is the boundary
 604 between the North Slope subterrane of the Arctic Alaska terrane (AAns in Figure 13) and
 605 the North America platformal strata in western Laurentia (NAp in Figure 13; Colpron et
 606 al., 2007). Although smaller in scale compared to the Kobuk Fault Zone and the Denali
 607 Fault System, the Porcupine Shear Zone appears to be the structural boundary between
 608 both the crustal and mantle velocity domains (C3 and C5 in Figures 10a and 13a and M3
 609 and M4 in Figure 10b and 13b). It also lies at a gradient in crustal thickness (Figure 11b).
 610 Thus the Porcupine Shear Zone is potentially a third strike-slip fault zone that connects to
 611 structural gradients in the mantle lithosphere.

612 In contrast, structural differences across the Kaltag Fault are primarily within the
 613 crustal range, while the structural signature of the Tintina Fault is primarily noticeable
 614 in the mantle lithosphere (Figure 13). The Kaltag Fault along the southern margin of the
 615 Brooks Range is a dextral strike-slip fault with more than 500 km slip in the late Cretaceous
 616 (Jones, 1980). Together with the Porcupine Shear Zone to its northeast, the Kaltag Fault
 617 has played an important role in the tectonic evolution of the Arctic Ocean Basin (Jones,
 618 1980). The velocity domains C3 and C4 are separated by a lineament of cluster boundaries
 619 along the eastern section of the Kaltag Fault, to the east of longitude 155°W (Figures
 620 10a and 13a). This is also the section with different tectonic terranes on the two sides of
 621 the fault (Figure 13a). The structural contrast further west across the fault is ambiguous,
 622 which is consistent with the fact that both sides of the fault belong to the same Koyukuk
 623 tectonic terrane (Figure 13a). The Tintina Fault in eastern Alaska and western Canada is
 624 a margin-parallel, dextral strike-slip fault zone with about 430 km horizontal displacement
 625 (e.g., Gabrielse et al., 2006). Audet et al. (2019) and Esteve et al. (2020) imaged a prominent
 626 contrast in seismic velocities in the upper mantle across the Tintina Fault in the western
 627 Yukon, suggesting the fault as a lithospheric-scale shear zone along the western margin of the
 628 North American continent. In the velocity clustering results, a small section of the Tintina
 629 Fault coincides with the NW-SE trending northeast edges of the M4 and M6 mantle domains
 630 (Figure 13b). In the individual N2020, F2019, J2018, and W2018 models, an anomalously
 631 high-velocity mantle lithosphere lies beneath the Yukon Stable Block, which is referred to
 632 by Esteve et al. (2020) as the Mackenzie craton. It is a fragment of the North American
 633 Platform on the northeast side of the Tintina Fault. However, the fault does not align with
 634 crustal cluster boundaries (Figure 13a). In summary, our analyses suggest that contrast in
 635 seismic structure occurs across a segment of the Tintina Fault in the mantle. This result,
 636 however, does not rule out a more laterally persistent contrast of seismic velocities at specific
 637 depths, since the clustering analysis considers the average pattern over the 40-120 km depth
 638 range.

639 Velocity domains C6 and M5 are both spatially correlated with the Wrangellia com-
 640 posite terrane, sampling both continental and oceanic lithosphere (Figure 13). At depths
 641 of 10-50 km, domain C6 contains varying amounts of both overriding crust and the oceanic
 642 lithosphere of the downgoing Yakutat Microplate. The average velocity below the depth of
 643 about 25 km is much lower than those for the adjacent C4-C5 domains (Figure 10c). This
 644 might be attributed to the inclusion of the overriding crust and the underlying thick (up to
 645 25 km) oceanic crust of the downgoing Yakutat Microplate (Eberhart-Phillips et al., 2004;
 646 Rondenay et al., 2010; Bauer et al., 2014; Chuang et al., 2017; Yang & Gao, 2020; Mann
 647 et al., 2022), resulting in combined crustal thicknesses that reach 55 km (Figure 11). As
 648 previously discussed in Section 5.2, at depths of 40-120 km in the M5 domain, the lower
 649 velocities than in other domains above the depth of 55 km likely reflect the thicker crust
 650 (Figure 10d, while the monotonically increasing velocities at greater depths sample mostly

651 the oceanic mantle lithosphere (Rondenay et al., 2010; Yang & Gao, 2020; Gama et al.,
 652 2022a; Mann et al., 2022).

653 5.4 Implications for the tectonics and geodynamics of the overriding continental 654 lithosphere

655 This study reveals a number of the features of the Alaskan crust and mantle structure
 656 of the overriding plate highlighted by the shear-wave velocity model clustering and the
 657 integration of the crustal thickness estimates. These seismic features shed light on the
 658 direction of future seismic, tectonic, and geodynamical studies, considering that variations
 659 in upper plate structure can have a first-order effect on both deformation in the overriding

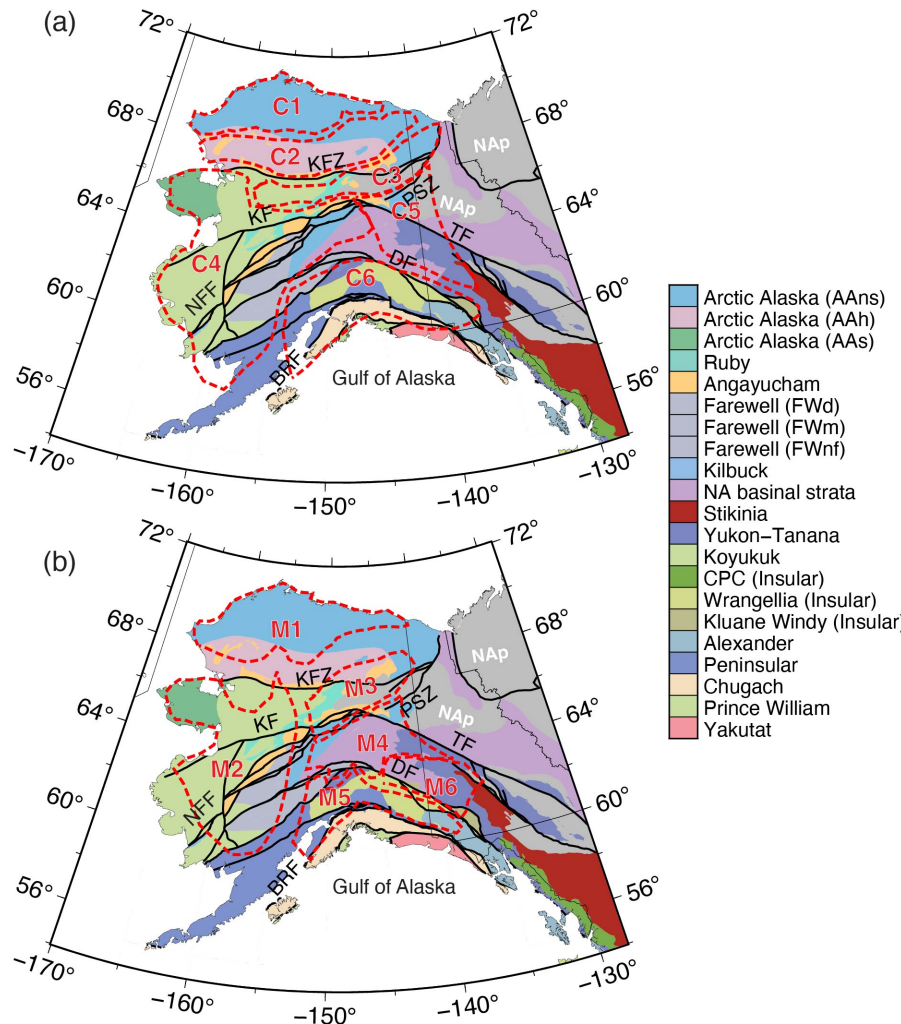


Figure 13. Comparison of velocity domains and major faults and tectonic terranes. (a) Major boundary lineaments of the velocity clusters (red dashed lines) and velocity domains (C1-C6) for 10-50 km clustering results overlapping on major fault lines and tectonic terrane maps. (b) Same as (a) but for mantle lithosphere at depths of 40-120 km (M1-M6). Labels of major faults are the same as in Figures 1b and 7 but are included here for easy reference. KFZ - Kobuk Fault Zone, KF - Kaltag Fault, PSZ - Porcupine Shear Zone, NFF - Nixon Fork-Iditarod Fault, TF - Tintina Fault, DF - Denali Fault System, BRF - Border Range Fault.

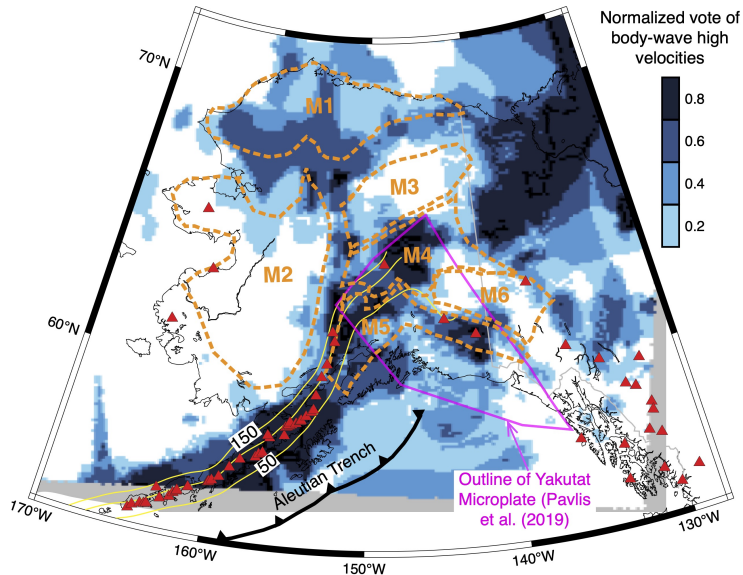


Figure 14. Comparison of mantle lithospheric velocity domains (M1-M6 within dashed outlines) and body-wave high velocities vote map at the depth of 100 km (colored background). The body-wave high-velocity vote map is from Pavlis et al. (this book), which contains more details on the body-wave vote maps. The slab depth contours (yellow lines with labeled depths in km) are from Slab 2.0 (Hayes et al., 2018). The outline of the Yakutat Microplate (magenta polygon) is from G. L. Pavlis et al. (2019). The red triangles are the active volcanoes same as in Figure 1a.

plate as well as slab dynamics (e.g. Sharples et al., 2014; Jadamec & Billen, 2012; Haynie & Jadamec, 2017).

One of the key findings from the synthesis is that some of the major faults and terrane boundaries spatially align with the margins of the crustal and mantle velocity domains that were independently determined from the velocity model clusters. Some of these correlations were previously documented, as in the case of the Denali and Kobuk faults (Rossi et al., 2006; Veenstra et al., 2006; Brennan et al., 2011; Ward & Lin, 2018; Allam et al., 2017; Miller et al., 2018; Martin-Short et al., 2018; Haney et al., 2020; Mann et al., 2022; Gama et al., 2022a, 2022b), but others, as in the case of the Porcupine Shear Zone, are newly revealed in this study. However, we have found that many boundaries of crustal and mantle velocity domains are not aligned. These results have the potential to add new constraints to tectonic models for how the complex mosaic of Alaskan terranes and faults interact (Bird, 1996; Kalbas et al., 2008; Elliott & Freymueller, 2020) and how they have evolved over time. A key next step will be to isolate how much of the mantle heterogeneity captured in the 40–120 km clusters actually lies within the mantle lithosphere, versus the underlying asthenosphere or subducting plate.

In the case of northernmost Alaska, it is already clear that the southern boundary of the M1 domain corresponds to a lithospheric-scale feature that separates the anomalously thick and high-velocity mantle lithosphere beneath the North Slope Arctic Alaska terrane from thinner lithosphere to the south. This observation poses a number of interesting questions. How has the North Slope M1 mantle lithosphere maintained its distinctive thickness and internal velocity structure over time? How much of the high mantle velocity is due to temperature, and how much could be attributed to mantle composition? A high-resolution model of mantle attenuation would be helpful in resolving this latter point, while the former requires input from geodynamic modeling efforts. Does the high velocity of the North

Slope mantle actually signify a fragment of cratonic mantle lithosphere, as suggested in some studies (Gama et al., 2022b), and does this indicate that the C1 domain is a remnant cratonic crust? The C2 domain, which contains the Brooks Range and lies over a transitional mantle with a variable lithospheric thickness, is comparable to many continental orogenic belts worldwide. How much does the anomalously thick and low-velocity (Figure 10c) C2 crust isostatically support the Brooks Range, versus isostatic contributions from the mantle? The geodynamic modeling studies thus far have led to significant advances in understanding the tectonics of Alaska and the surrounding regions. However, most of the three-dimensional finite-element models spanning the entirety of mainland Alaska and northwestern Canada have incorporated a laterally variable lithospheric structure in the overriding plate, though focusing on the deformation in central and southern Alaska (Bird, 1996; Kalbas et al., 2008; Jadamec & Billen, 2010; Jadamec et al., 2013). These models are limited by either not including the asthenosphere (e.g. Bird, 1996; Kalbas et al., 2008) or essentially fixing the North Slope region to the model boundary and, thus, limiting the lithospheric motion in northernmost Alaska (e.g. Jadamec & Billen, 2010; Jadamec et al., 2013). Whereas, numerical models of Alaska that involve the deformation of northern Alaska are limited by the thin viscous sheet approach without a dynamic asthenosphere (e.g. Finzel et al., 2015). Therefore, this makes it difficult for these models to self-consistently assess mantle flow and Brooks Range equilibrium, for example. Nonetheless, the new EarthScope data and results will foster continued rich model development and geodynamic discovery in Alaska and northwestern Canada.

The alignment of some major fault systems (Denali, Kobuk, Porcupine Shear Zone, Kaltag, Tintina) with the margins of the crustal and/or mantle velocity domains also has the potential to provide new constraints on the depth extent and dynamics of strike-slip faulting in the continental lithosphere. Such correlations may indicate that lateral variations in the strength of the crust and mantle lithosphere play a role in determining and maintaining the location of the fault zone, as has been suggested globally (e.g., Molnar & Dayem, 2010; Dayem et al., 2009). The fault zones and the local reduction in strength that they represent in turn have a major impact on the dynamics of the overriding plate in Alaska (e.g., Haynie & Jadamec, 2017). For example, the Wrangell block, a region between the Alaska megathrust to the south and the Denali fault to the north, moves semi-independently from the inboard North American plate of interior Alaska (Lahr & Plafker, 1980). GPS data analyses indicate the northwest-directed counter-clockwise motion of the Wrangell block (e.g. Elliott & Freymueller, 2020). Geodynamic modeling demonstrates that the sub-parallelism of the plate boundary corner with the inboard Denali fault, allows northwest-directed flat slab subduction of the Pacific-Wrangell plate to drive the overriding Wrangell block from below, with the Denali fault strength modulating its rotation (Jadamec et al., 2013; Haynie & Jadamec, 2017). In the future, high-resolution studies of seismic velocity (both isotropic and anisotropic) in the vicinity of the major fault systems of Alaska have the potential to help constrain this process and the degree to which strike-slip deformation remains horizontally localized in the deep crust and mantle lithosphere.

The results of this study also highlight the first-order effect of the subduction of the Yakutat terrane in southern Alaska, which is expressed as the thick crust evident in the C6 and the top of the M5 domains, and the structural complexity in the M4 domain. The average crustal velocity profile in the C6 domain (which reflects continental crust over the subducting plate) provides new constraints on the buoyancy of the Yakutat crust. These constraints will be useful for lithospheric-scale (e.g., Finzel et al., 2015; McConeghy, Flesch, & Elliott, 2022) and mantle-scale (e.g., Jadamec & Billen, 2010, 2012; Jadamec et al., 2013; Haynie & Jadamec, 2017) geodynamical models of subduction in Alaska and its impact on the overriding continental lithosphere. The crustal seismic velocities and thickness constraints synthesized in this study could also help to better design representative models of upper plate dynamics (Torne et al., 2019) and models of plateau subduction to examine the effects of plateau subduction-collision on long-term plate boundary evolution (e.g., Koons et

738 al., 2010; Haynie, 2019; Moresi et al., 2014) and the role of eclogitization of the subducting
 739 plateau with depth (Arrial & Billen, 2013).

740 6 Conclusions

741 A primary goal of this study was to synthesize the results of existing seismic studies
 742 to create tools for studying the upper plate lithosphere in Alaska that could be used by a
 743 broad range of researchers. To that end, this study provides:

- 744 • Maps showing the results of seven studies of crustal thickness based on receiver func-
 745 tions;
- 746 • A crustal thickness reference map that synthesizes the three of these crustal thick-
 747 ness models that provided at least semi-continuous sampling, and that accounts for
 748 complexity due to multiple crustal layers in southern Alaska;
- 749 • Maps of eight published shear-velocity models for Alaska;
- 750 • Domain boundaries determined through clustering analysis and their corresponding
 751 velocity profiles from the individual shear-velocity models;
- 752 • Composite domain boundaries and mean velocity profiles that represent the combi-
 753 nation of all shear-velocity models.

754 Through the clustering analysis, six distinct velocity domains are identified in the
 755 crustal depth range (10-50 km) and in the mantle (40-120 km), without considering informa-
 756 tion on the distribution of terranes and faults. However, the velocity domain boundaries are
 757 in many cases close to terrane boundaries and/or major fault systems, indicating feedback
 758 between the crust (and even mantle structure) and geologic features at the surface. These
 759 correlations include both crust and mantle domain boundaries that align with: the Den-
 760 nali Fault System and the boundary between the Wrangellia composite terrane and interior
 761 Alaska; the Kobuk fault and the southern boundary of the Hammond-Coldfoot subterrane in
 762 northern Alaska; the southern boundary of the North Slope subterrane in northern Alaska;
 763 and the Porcupine Shear Zone in northern Alaska. The Kaltag Fault and the Tintina Fault
 764 at least partially align with the crustal and mantle velocity domain boundaries, respectively.

765 The crust and mantle velocity domains clearly outline three major structural domains
 766 within the upper plate of Alaska: the anomalously thick crust associated with the subduction
 767 of the Yakutat terrane in the south; the thin lithosphere above a well-defined low-velocity
 768 lithosphere over much of interior Alaska; an anomalously thick crust and a transition to
 769 thicker lithosphere beneath the Brooks Range; and a thick crust above very thick and high-
 770 velocity mantle lithosphere beneath the North Slope subterrane in northernmost Alaska.
 771 The western edge of the thick lithosphere beneath the MacKenzie craton in Canada is also
 772 detected as a mantle domain boundary.

773 Availability Statement

774 Seismic network information is available from the IRIS Data Management Center
 775 (<https://ds.iris.edu/ds/nodes/dmc/>) and the International Federation of Digital Seis-
 776 mograph Networks (<https://www.fdsn.org>). The network codes and digital object iden-
 777 tifiers (DOI) are: 5C (DOI:10.7914/SN/5C_2009), 7C (DOI:10.7914/SN/7C_2015), AK
 778 (DOI:10.7914/SN/AK), AT (DOI:10.7914/SN/AT), AV (DOI:10.7914/SN/AV), CN (DOI:
 779 10.7914/SN/CN), II (DOI:10.7914/SN/II), IM (no DOI), IU (DOI:10.7914/SN/IU), PP
 780 (no DOI), PQ (DOI:10.7914/SN/PQ), TA (DOI:10.7914/SN/TA), US (DOI:10.7914/SN/
 781 US), XE (DOI:10.7914/SN/XE_1999), XF (DOI:10.7914/SN/XF_2009), XL (DOI:10.7914/
 782 SN/XL_2008), XM (DOI:10.7914/SN/XM_2011), XN (DOI:10.7914/SN/XN_2003), XO (DOI:
 783 10.7914/SN/XO_2018), XR (DOI:10.7914/SN/XR_2004), XV (DOI:10.7914/SN/XV_2014),
 784 XZ (DOI:10.7914/SN/XZ_2005), YE (DOI:10.7914/SN/YE_2007), YG (DOI:10.7914/SN/
 785 YG_2016), YM (DOI:10.7914/SN/YM_2002), YO (DOI:10.7914/SN/YO_2010), YV (DOI:10

786 .7914/SN/YV_2006), Z5 (DOI:10.7914/SN/Z5_2018), ZE (DOI:10.7914/SN/ZE_2015). See
787 Table S1 in the supplement for detailed descriptions and references of the seismic net-
788 works. The seismic models are downloaded from IRIS Earth Model Collaboration (<https://doi.org/10.17611/DP/EMC.1>) or directly provided by the corresponding authors. The clus-
789 tering analysis of the seismic velocity models is conducted using *SeisGo* (<https://doi.org/10.5281/zenodo.5873724>). The electronic supplementary file for Figures S1-S9 and Ta-
790 ble S1, the velocity domain outlines, the key cluster boundaries (cluster lineaments), the
791 average crustal thickness models, and the Python Jupyter notebook to plot the cluster do-
792 mains are archived on Zenodo and can be downloaded from <https://doi.org/10.5281/zenodo.7516572>.
793
794

796 Acknowledgments

797 This paper grew out of discussions at the UNAVCO Alaska EarthScope and Beyond Vir-
798 tual Seminar Series in Spring 2021 and the paired EarthScope Alaska and Beyond Virtual
799 Workshop in May 2021, which were supported by the National Science Foundation and
800 the National Aeronautics and Space Administration. The authors thank the conference
801 organizers, Jeffrey Freymueller, Julie Elliot, Sarah Roeske, and Rick Aster, as well as par-
802 ticipants at the meeting for thoughtful discussions. We are also grateful to R. Martin-Short,
803 M. Miller, and A. Li for directly providing their models, to the other authors who made
804 their models available through the IRIS EMC, and to the field teams for deploying and
805 maintaining the seismic networks used by the synthesized seismic models. This work is
806 supported by the startup funding at Purdue University to X. Yang, NSF CAREER Grant
807 NSF-EAR 1945513 to M. Jadamec, NSF EAR-2052558 to S. S. Wei, NSF EAR-2053042
808 and Woods Hole Oceanographic Institution OBS Instrument Center Postdoctoral Scholar-
809 ship to M. E. Mann, and NSF EAR-1829401 to K. M. Fischer. **Author Contributions:**
810 X. Yang contributed to supervision, funding acquisition, data curation, methodology, for-
811 mal analysis, interpretation, and writing of the original draft. M. Mann and K. Fischer
812 contributed to data curation, methodology, formal analysis, interpretation, and writing of
813 the original draft. M. Jadamec contributed to the writing of the original draft. S. Wei
814 and A. Schaeffer contributed to methodology. G. Pavlis contributed to formal analysis. All
815 authors contributed to the conceptualization, interpretation, and reviewing and editing of
816 the manuscript.

817 **References**

- 818 Ai, Y., Zhao, D., Gao, X., & Xu, W. (2005, 6). The crust and upper mantle discontinuity
 819 structure beneath Alaska inferred from receiver functions. *Physics of the Earth and*
 820 *Planetary Interiors*, *150*, 339-350. doi: 10.1016/J.PEPI.2004.12.002
- 821 Allam, A. A., Schulte-Pelkum, V., Ben-Zion, Y., Tape, C., Ruppert, N., & Ross, Z. E. (2017,
 822 11). Ten kilometer vertical moho offset and shallow velocity contrast along the denali
 823 fault zone from double-difference tomography, receiver functions, and fault zone head
 824 waves. *Tectonophysics*, *721*, 56-69. doi: 10.1016/J.TECTO.2017.09.003
- 825 Arrial, P.-A., & Billen, M. I. (2013). Influence of geometry and eclogitization on oceanic
 826 plateau subduction. *Earth and Planetary Science Letters*, *363*, 34-43.
- 827 Audet, P., Currie, C. A., Schaeffer, A. J., & Hill, A. M. (2019). Seismic evidence for litho-
 828 spheric thinning and heat in the northern canadian cordillera. *Geophysical Research*
 829 *Letters*, *46*(8), 4249 - 4257. Retrieved from <https://proxyub.uits.iu.edu/login?url=https://search.ebscohost.com/login.aspx?direct=true&db=geh&AN=2019-059384&site=ehost-live&scope=site>
- 832 Avé Lallement, H. G., Gottschalk, R. R., Sisson, V. B., & Oldow, J. S. (1998). Structural
 833 analysis of the Kobuk fault zone, north-central Alaska. *Special Paper of the Geological*
 834 *Society of America*, *324*, 261-268. doi: 10.1130/0-8137-2324-8.261
- 835 Barcheck, G., Abers, G. A., Adams, A. N., Bécel, A., Collins, J., Gaherty, J. B., ... Wor-
 836 thington, L. L. (2020, 11). The alaska amphibious community seismic experiment.
 837 *Seismological Research Letters*, *91*, 3054-3063. doi: 10.1785/0220200189
- 838 Batir, J. F., Blackwell, D. D., & Richards, M. C. (2016). Heat flow and temperature-depth
 839 curves throughout Alaska: Finding regions for future geothermal exploration. *Journal*
 840 *of Geophysics and Engineering*, *13*, 366-377. doi: 10.1088/1742-2132/13/3/366
- 841 Bauer, M. A., Pavlis, G. L., & Landes, M. (2014). Subduction geometry of the yakutat
 842 terrane, southeastern alaska. *Geosphere*, *10*, 1161-1176. doi: 10.1130/GES00852.1
- 843 Benowitz, J. A., Roeske, S. M., Regan, S. P., Waldien, T. S., Elliott, J. L., & O'Sullivan,
 844 P. B. (2022, 6). Large-scale, crustal-block vertical extrusion between the hines creek
 845 and denali faults coeval with slip localization on the denali fault since ca. 45 ma, hayes
 846 range, alaska, usa. *Geosphere*, *18*, 1030-1054. Retrieved from <https://doi.org/10.1130/GES02466.1>. doi: 10.1130/GES02466.1
- 848 Berg, E. M., Lin, F. C., Allam, A., Schulte-Pelkum, V., Ward, K. M., & Shen, W.
 849 (2020, 2). Shear velocity model of Alaska via joint inversion of rayleigh wave el-
 850 lipticity, phase velocities, and receiver functions across the Alaska transportable ar-
 851 ray. *Journal of Geophysical Research: Solid Earth*, *125*, e2019JB018582. Retrieved
 852 from <https://onlinelibrary.wiley.com/doi/full/10.1029/2019JB018582> doi:
 853 10.1029/2019JB018582
- 854 Bird, P. (1996). Computer simulations of Alaskan tectonics. *Tectonics*, *15*(2), 225-236.
- 855 Bird, P. (2003). An updated digital model of plate boundaries. *Geochemistry Geophysics*
 856 *Geosystems*, *4*(3), 1027. doi: 10.1029/2001GC000252
- 857 Bostock, M. G. (2013, 12). The moho in subduction zones. *Tectonophysics*, *609*, 547-557.
 858 doi: 10.1016/J.TECTO.2012.07.007
- 859 Brennan, P. R. K., Gilbert, H., Ridgway, K. D., Brennan, P. R. K., Gilbert, H., & Ridgway,
 860 K. D. (2011, 4). Crustal structure across the central Alaska range: Anatomy of a
 861 mesozoic collisional zone. *Geochemistry, Geophysics, Geosystems*, *12*, 4010. Retrieved
 862 from <https://onlinelibrary.wiley.com/doi/full/10.1029/2011GC003519> doi:
 863 10.1029/2011GC003519
- 864 Chuang, L., Bostock, M., Wech, A., & Plourde, A. (2017, 7). Plateau subduction,
 865 intraslab seismicity, and the denali (alaska) volcanic gap. *Geology*, *45*, 647-650.
 866 Retrieved from <https://pubs.geoscienceworld.org/geology/article/45/7/647-650/207873> doi: 10.1130/G38867.1
- 868 Clarke, T. J., & Silver, P. G. (1991, 1). A procedure for the systematic interpretation of body
 869 wave seismograms—i. application to moho depth and crustal properties. *Geophysical*
 870 *Journal International*, *104*, 41-72. Retrieved from <https://academic.oup.com/gji/article/104/1/41/569865> doi: 10.1111/J.1365-246X.1991.TB02493.X

- 872 Colpron, M., Nelson, J. L., & Murphy, D. C. (2007, 4). Northern cordilleran terranes
 873 and their interactions through time. *GSA Today*, 17, 4. Retrieved from <http://www.geosociety.org/gsatoday/archive/17/4/pdf/i1052-5173-17-4-4.pdf> doi:
 874 10.1130/GSAT01704-5A.1
- 875 Coney, P. J., Jones, D. L., & Monger, J. W. (1980). Cordilleran suspect terranes. *Nature*
 876 1980 288:5789, 288, 329-333. Retrieved from <https://www.nature.com/articles/288329a0> doi: 10.1038/288329a0
- 877 Daly, K. A., Abers, G. A., Mann, M. E., Roecker, S., & Christensen, D. H. (2021,
 878 11). Subduction of an oceanic plateau across southcentral Alaska: High-resolution
 879 seismicity. *Journal of Geophysical Research: Solid Earth*, 126. Retrieved from
 880 <https://onlinelibrary.wiley.com/doi/10.1029/2021JB022809> doi: 10.1029/
 881 2021JB022809
- 882 Dayem, K. E., Houseman, G. A., & Molnar, P. (2009, 6). Localization of shear along a
 883 lithospheric strength discontinuity: Application of a continuous deformation model
 884 to the boundary between Tibet and the Tarim Basin. *Tectonics*, 28. Retrieved
 885 from <https://onlinelibrary.wiley.com/doi/full/10.1029/2008TC002264> doi:
 886 10.1029/2008TC002264
- 887 Delph, J. R., Shimizu, K., & Ratschbacher, B. C. (2021, 7). The architecture of the
 888 southern Puna Magmatic System: Integrating seismic and petrologic observations
 889 with geochemical modeling. *Journal of Geophysical Research: Solid Earth*, 126,
 890 e2020JB021550. Retrieved from <https://onlinelibrary.wiley.com/doi/full/10.1029/2020JB021550> doi: 10.1029/2020JB021550
- 891 DeMets, C., Gordon, R. G., Argus, D. F., & Stein, S. (1994). Effect of recent revisions to
 892 the geomagnetic reversal time scale on estimates of current plate motions. *Geophysical*
 893 *Research Letters*, 218(207-237), 2191-2194.
- 894 Eberhart-Phillips, D., Christensen, D. H., Brocher, T. M., Dutta, U., Hansen, R. J., &
 895 Ratchkovski, N. A. (2004). Imaging the transition from aleutian subduction to yakutat
 896 collision in central Alaska, with local earthquakes and active source data. *Geological*
 897 *Society of New Zealand Miscellaneous Publication*, 117A, 27.
- 898 Eberhart-Phillips, D., Haeussler, P. J., Freymueller, J. T., Frankel, A. D., Rubin, C. M.,
 899 Craw, P., ... Wallace, W. K. (2003). The 2002 Denali Fault Earthquake: A large
 900 magnitude, slip-partitioned event. *Science*, 300, 1112-1118.
- 901 Elliott, J., & Freymueller, J. T. (2020). A block model of present-day kinematics of Alaska
 902 and western Canada. *Journal of Geophysical Research: Solid Earth*, 125, 1-30. doi:
 903 10.1029/2019JB018378
- 904 Enkelmann, E., Zeitler, P., Garver, J., Pavlis, T., & Hooks, B. (2010). The thermochronological
 905 record of tectonic and surface process interaction at the yakutat-north american
 906 collision zone in southeast alaska. *American Journal of Science*, 310(4), 231-260.
- 907 Esteve, C., Audet, P., Schaeffer, A. J., Schutt, D., Aster, R. C., & Cubley, J. (2020). The up-
 908 per mantle structure of northwestern canada from teleseismic body wave tomography.
 909 *Journal of Geophysical Research: Solid Earth*, 125(2).
- 910 Esteve, C., Gosselin, J., Audet, P., Schaeffer, A. J., Schutt, D., & Aster, R. C. (2021).
 911 Surface-wave tomography of the Northern Canadian Cordillera using earthquake
 912 Rayleigh wave group velocities. *Journal of Geophysical Research*, 126. Retrieved
 913 from <https://doi.org/10.1029/2021JB021960>
- 914 Falkowski, S., & Enkelmann, E. (2016, 8). Upper-crustal cooling of the wrangellia com-
 915 posite terrane in the northern st. elias mountains, western canada. *Lithosphere*,
 916 8, 359-378. Retrieved from <http://pubs.geoscienceworld.org/gsa/lithosphere/article-pdf/8/4/359/3040051/359.pdf> doi: 10.1130/L508.1
- 917 Feng, L., & Ritzwoller, M. H. (2019). A 3-d shear velocity model of the crust and uppermost
 918 mantle beneath Alaska including apparent radial anisotropy. *Journal of Geophysical*
 919 *Research: Solid Earth*, 124, 10468-10497. doi: 10.1029/2019JB018122
- 920 Finzel, E. S., Flesch, L. M., Ridgway, K. D., Holt, W. E., & Ghosh, A. (2015). Surface
 921 motions and intraplate continental deformation in Alaska driven by mantle flow.
 922 *Geophysical Research Letters*, 42(11), 4350 - 4358. Retrieved from <https://doi.org/10.1029/2015GL064810>
- 923

- proxyiub.uits.iu.edu/login?url=https://search.ebscohost.com/login.aspx?direct=true&db=geh&AN=2015-086771&site=ehost-live&scope=site
- Fuis, G. S., Ambos, E. L., Mooney, W. D., Christensen, N. I., & Geist, E. (1991). Crustal structure of accreted terranes in southern Alaska, Chugach Mountains and Copper River basin, from seismic refraction results. *J. of Geophys. Res.*, *96*, 4187-4227.
- Fuis, G. S., Levander, A. R., Lutter, W. J., Wissinger, E. S., Moore, T. E., & Christensen, N. I. (1995). Seismic images of the brooks range, arctic Alaska, reveal crustal-scale duplexing. *Geology*, *23*, 65-68. Retrieved from <http://pubs.geoscienceworld.org/gsa/geology/article-pdf/23/1/65/4665573/i0091-7613-23-1-65.pdf>
- Fuis, G. S., Moore, T. E., Plafker, G., Brocher, T. M., Fisher, M. A., Mooney, W. D., ... Ruppert, N. A. (2008). Trans-Alaska crustal transect and continental evolution involving subduction underplating and synchronous foreland thrusting. *Geology*, *36*, 267-270. doi: 10.1130/G24257A.1
- Fuis, G. S., Murphy, J. M., Lutter, W. J., Moore, T. E., Bird, K. J., & Christensen, N. I. (1997, 9). Deep seismic structure and tectonics of northern Alaska: Crustal-scale duplexing with deformation extending into the upper mantle. *Journal of Geophysical Research: Solid Earth*, *102*, 20873-20896. Retrieved from <https://onlinelibrary.wiley.com/doi/full/10.1029/96JB03959> doi: 10.1029/96JB03959
- Fuis, G. S., & Plafker, G. (1991, 3). Evolution of deep structure along the trans-Alaska crustal transect, chugach mountains and copper river basin, southern alaska. *Journal of Geophysical Research: Solid Earth*, *96*, 4229-4253. Retrieved from <https://onlinelibrary.wiley.com/doi/full/10.1029/90JB02276> doi: 10.1029/90JB02276
- Gabrielse, H., Murphy, D. C., & Mortensen, J. K. (2006). Cretaceous and Cenozoic dextral orogen-parallel displacements, magmatism, and paleogeography, north-central Canadian Cordillera. In J. Haggart & J. E. R.J.Monger (Eds.), *Paleogeography of the north american cordillera: Evidence for and against large-scale displacements: Geological association of canada special paper* (Vol. 46, p. 255-276). Retrieved from <https://www.researchgate.net/publication/285873017>
- Gama, I., Fischer, K. M., Dalton, C. A., & Eilon, Z. (2022b, 12). Variations in lithospheric thickness across the denali fault and in northern Alaska. *Geophysical Research Letters*, *e2022GL101256*. Retrieved from <https://onlinelibrary.wiley.com/doi/full/10.1029/2022GL101256> doi: 10.1029/2022GL101256
- Gama, I., Fischer, K. M., Eilon, Z., Krueger, H. E., Dalton, C. A., & Flesch, L. M. (2021, 4). Shear-wave velocity structure beneath Alaska from a bayesian joint inversion of sp receiver functions and rayleigh wave phase velocities. *Earth and Planetary Science Letters*, *560*, 116785. doi: 10.1016/J.EPSL.2021.116785
- Gama, I., Fischer, K. M., & Hua, J. (2022a, 10). Mapping the lithosphere and asthenosphere beneath Alaska with sp converted waves. *Geochemistry, Geophysics, Geosystems*, *23*, e2022GC010517. Retrieved from <https://onlinelibrary.wiley.com/doi/10.1029/2022GC010517> doi: 10.1029/2022GC010517
- Gou, T., Zhao, D., Huang, Z., & Wang, L. (2019). Aseismic deep slab and mantle flow beneath Alaska: Insight from anisotropic tomography. *Journal of Geophysical Research: Solid Earth*, *124*, 1700-1724. doi: 10.1029/2018JB016639
- Grantz, A., May, S. D., & Hart, P. E. (1994). Geology of the Arctic continental margin of Alaska. In *The Geology of Alaska* (Vols. DNAG, Geology of North America). Geological Society of America. doi: 10.1130/DNAG-GNA-G1.17
- Haney, M. M., Ward, K. M., Tsai, V. C., & Schmandt, B. (2020, 11). Bulk structure of the crust and upper mantle beneath Alaska from an approximate rayleigh-wave dispersion formula. *Seismological Research Letters*, *91*, 3064-3075. Retrieved from <https://pubs.geoscienceworld.org/ssa/srl/article/91/6/3064/589671/Bulk-Structure-of-the-Crust-and-Upper-Mantle> doi: 10.1785/0220200162
- Hayes, G. P., Moore, G. L., Portner, D. E., Hearne, M., Flamme, H., Furtney, M., & Smoczyk, G. M. (2018). Slab2, a comprehensive subduction zone geometry model. *Science*, *362*, 58-61. doi: 10.1126/science.aat4723

- 982 Haynie, K. L. (2019). *Controls of flat slab versus oceanic plateau subduction on overriding*
 983 *plate deformation in south-central alaska* (Unpublished doctoral dissertation). State
 984 University of New York at Buffalo.
- 985 Haynie, K. L., & Jadamec, M. A. (2017, 7). Tectonic drivers of the Wrangell block:
 986 Insights on fore-arc sliver processes from 3-D geodynamic models of Alaska. *Tectonics*,
 987 36, 1180-1206. Retrieved from <https://onlinelibrary.wiley.com/doi/10.1002/2016TC004410> doi: 10.1002/2016TC004410
- 989 Hubbard, R. J., Edrich, S. P., & Rattey, R. P. (1987, 2). Geologic evolution and hydrocarbon
 990 habitat of the ‘Arctic Alaska Microplate’. *Marine and Petroleum Geology*, 4, 2-34.
 991 doi: 10.1016/0264-8172(87)90019-5
- 992 Hyndman, R. D., Currie, C. A., & Mazzotti, S. P. (2005). Subduction zone backarcs,
 993 mobile belts, and orogenic heat. *Geological Society of America Today*, 15(23). doi:
 994 10.1130/1052-5173
- 995 Jadamec, M. A., & Billen, M. I. (2010). Reconciling surface plate motions and rapid
 996 three-dimensional flow around a slab edge. *Nature*, 465, 338-342.
- 997 Jadamec, M. A., & Billen, M. I. (2012). The role of rheology and slab shape on rapid
 998 mantle flow: Three-dimensional numerical models of the Alaska slab edge. *Journal of*
 999 *Geophysical Research: Solid Earth*, 117, 1-20. doi: 10.1029/2011JB008563
- 1000 Jadamec, M. A., Billen, M. I., & Roeske, S. M. (2013). Three-dimensional numerical
 1001 models of flat slab subduction and the Denali fault driving deformation in south-central
 1002 Alaska. *Earth and Planetary Science Letters*, 376, 29-42. Retrieved from <http://dx.doi.org/10.1016/j.epsl.2013.06.009> doi: 10.1016/j.epsl.2013.06.009
- 1004 Jiang, C., Schmandt, B., Ward, K. M., Lin, F., & Worthington, L. L. (2018, 10). Upper
 1005 mantle seismic structure of Alaska from rayleigh and s wave tomography. *Geophysical*
 1006 *Research Letters*, 45, 10,350-10,359. Retrieved from <https://onlinelibrary.wiley.com/doi/10.1029/2018GL079406> doi: 10.1029/2018GL079406
- 1008 Jones, P. B. (1980). Evidence from canada and alaska on plate tectonic evolution of the
 1009 arctic ocean basin. *Nature*, 285, 215-217. Retrieved from <https://www.nature.com/articles/285215a0> doi: 10.1038/285215a0
- 1011 Kalbas, J. L., Freed, A. M., & Ridgway, K. D. (2008). Contemporary fault mechanics in
 1012 southern Alaska. *Geophysical Monograph Series*, 179, 321–336.
- 1013 Kim, Y., Abers, G. A., Li, J., Christensen, D., Calkins, J., & Rondenay, S. (2014,
 1014 3). Alaska Megathrust 2: Imaging the megathrust zone and Yakutat/Pacific plate
 1015 interface in the Alaska subduction zone. *Journal of Geophysical Research: Solid*
 1016 *Earth*, 119, 1924-1941. Retrieved from <https://onlinelibrary.wiley.com/doi/full/10.1002/2013JB010581> doi: 10.1002/2013JB010581
- 1018 Koons, P. O., Hooks, B. P., Pavlis, T., Upton, P., & Barker, A. D. (2010, 8). Three-
 1019 dimensional mechanics of yakutat convergence in the southern alaskan plate corner.
 1020 *Tectonics*, 29. Retrieved from <https://agupubs.onlinelibrary.wiley.com/doi/10.1029/2009TC002463> doi: 10.1029/2009TC002463
- 1022 Lahr, J. C., & Plafker, G. (1980). Holocene Pacific-North American plate interaction in
 1023 southern Alaska: implications for the Yakataga seismic gap. *Geology*, 8, 483-486.
- 1024 Langston, C. A. (1977, 6). Corvallis, oregon, crustal and upper mantle receiver structure
 1025 from teleseismic p and s waves. *Bulletin of the Seismological Society of America*, 67,
 1026 713-724. doi: 10.1785/BSSA0670030713
- 1027 Lekic, V., & Romanowicz, B. (2011, 8). Tectonic regionalization without a priori information:
 1028 A cluster analysis of upper mantle tomography. *Earth and Planetary Science*
 1029 *Letters*, 308, 151-160. doi: 10.1016/J.EPSL.2011.05.050
- 1030 Liu, C., Zhang, S., Sheehan, A. F., & Ritzwoller, M. H. (2022, 11). Surface wave isotropic
 1031 and azimuthally anisotropic dispersion across Alaska and the Alaska-Aleutian subduc-
 1032 tion zone. *Journal of Geophysical Research: Solid Earth*, 127, e2022JB024885. Re-
 1033 trieval from <https://onlinelibrary.wiley.com/doi/10.1029/2022JB024885> doi:
 1034 10.1029/2022JB024885
- 1035 Mann, M. E., Abers, G. A., Daly, K. A., & Christensen, D. H. (2022, 1). Subduction of
 1036 an oceanic plateau across southcentral Alaska: Scattered-wave imaging. *Journal of*

- 1092 proxyiub.uits.iu.edu/login?url=https://search.ebscohost.com/login.aspx
 1093 ?direct=true&db=geh&AN=2019-091128&site=ehost-live&scope=site
- 1094 Plafker, G., & Berg, H. C. (1994, 4). Overview of the geology and tectonic evolution of
 1095 Alaska. In (p. 989-1021). Geological Society of America. Retrieved from <https://pubs.geoscienceworld.org/books/book/875/chapter/4867358/> doi: 10.1130/DNAG-
 1097 -GNA-G1.989
- 1098 Plafker, G., Gilpin, L. M., & Lahr, J. C. (1994). Plate 12: Neotectonic Map of Alaska. In
 1099 G. Plafker & H. Berg (Eds.), *The geology of north america* (Vols. G1, The Geology of
 1100 Alaska). Boulder, Colo.: Geological Society of America.
- 1101 Plafker, G., Moore, J. C., & Winkler, G. R. (1994). Geology of the southern Alaska margin.
 1102 In G. Plafker & H. Berg (Eds.), *The geology of north america* (Vols. G1, The Geology
 1103 of Alaska, p. 389-449). Boulder, Colo.: Geological Society of America.
- 1104 Rondenay, S., Abers, G. A., & van Keken, P. E. (2008, 4). Seismic imaging of subduction
 1105 zone metamorphism. *Geology*, *36*, 275-278. doi: 10.1130/G24112A.1
- 1106 Rondenay, S., Montési, L. G., & Abers, G. A. (2010, 8). New geophysical insight into the
 1107 origin of the denali volcanic gap. *Geophysical Journal International*, *182*, 613-630.
 1108 Retrieved from <https://academic.oup.com/gji/article/182/2/613/568363> doi:
 1109 10.1111/J.1365-246X.2010.04659.X
- 1110 Rossi, G., Abers, G. A., Rondenay, S., & Christensen, D. H. (2006, 9). Unusual mantle
 1111 poisson's ratio, subduction, and crustal structure in central Alaska. *Journal of Geophysical Research: Solid Earth*, *111*, 9311. Retrieved from <https://onlinelibrary.wiley.com/doi/full/10.1029/2005JB003956> doi: 10.1029/2005JB003956
- 1112 Ruppert, N. A., & West, M. E. (2020, 3). The impact of USArray on earthquake monitoring
 1113 in Alaska. *Seismological Research Letters*, *91*, 601-610. doi: 10.1785/0220190227
- 1114 Schaeffer, A. J., & Lebedev, S. (2015, 1). Global heterogeneity of the lithosphere and
 1115 underlying mantle: A seismological appraisal based on multimode surface-wave dispersion
 1116 analysis, shear-velocity tomography, and tectonic regionalization. *The Earth's Heterogeneous Mantle: A Geophysical, Geodynamical, and Geochemical Perspective*,
 1117 3-46. Retrieved from [https://link.springer.com/chapter/10.1007/978-3-319-15627-9_1/FIGURES/19](https://link.springer.com/chapter/10.1007/978-3-319-15627-9_1)
 1118 doi: 10.1007/978-3-319-15627-9_1
- 1119 Searcy, C. K., Christensen, D. H., & Zandt, G. (1996, 2). Velocity structure beneath
 1120 college station Alaska from receiver functions. *Bulletin of the Seismological Society of
 1121 America*, *86*, 232-241. doi: 10.1785/BSSA08601A0232
- 1122 Seton, M., Müller, R. D., Zahirovic, S., Williams, S., Wright, N. M., Cannon, J., ... McGirr,
 1123 R. (2020). A global data set of present-day oceanic crustal age and seafloor spreading
 1124 parameters. *Geochemistry, Geophysics, Geosystems*, *21*(10), e2020GC009214.
- 1125 Sharples, W., Jadamec, M. A., Moresi, L. N., & Capitanio, F. (2014). Overriding plate
 1126 controls on subduction evolution. *Journal of Geophysical Research*, *119*, 6684-6704.
 1127 doi: 10.1002/2014JB011163
- 1128 Silberling, N. J., Jones, D. L., Monger, J. W. H., Coney, P. J., Berg, H. C., & Plafker, G.
 1129 (1994). Plate 3: Lithotectonic terrane map of Alaska and adjacent parts of Canada. In
 1130 G. Plafker & H. Berg (Eds.), *The Geology of North America* (Vols. G1, The Geology
 1131 of Alaska). Boulder, Colo.: Geological Society of America.
- 1132 Strauss, J. V., Macdonald, F. A., Taylor, J. F., Repetski, J. E., & McClelland, W. C.
 1133 (2013). Laurentian origin for the North Slope of Alaska: Implications for the tectonic
 1134 evolution of the arctic. *Lithosphere*, *5*, 477-482. doi: 10.1130/L284.1
- 1135 Tavenard, R., Faouzi, J., Vandewiele, G., Divo, F., Androz, G., Holtz, C., ... Woods,
 1136 E. (2020). Tslearn, a machine learning toolkit for time series data. *Journal of Machine
 1137 Learning Research*, *21*(118), 1-6. Retrieved from <http://jmlr.org/papers/v21/20-091.html>
- 1138 Torne, M., Jimenez-Munt, I., Verges, J., Fernandez, M., Carballo, A., & Jadamec, M. A.
 1139 (2019). Regional crustal and lithospheric thickness model for Alaska, the Chukchi
 1140 Shelf, and the inner and outer Bering Shelves. *Geophysical Journal International*,
 1141 *ggz424*. doi: <https://doi.org/10.1093/gji/ggz424>
- 1142 Tozer, B., Sandwell, D. T., Smith, W. H., Olson, C., Beale, J., & Wessel, P. (2019). Global
 1143

- 1147 bathymetry and topography at 15 arc sec: Srtm15+. *Earth and Space Science*, 6(10),
 1148 1847–1864.
- 1149 Veenstra, E., Christensen, D. H., Abers, G. A., & Ferris, A. (2006, 9). Crustal thickness
 1150 variation in south-central Alaska. *Geology*, 34, 781-784. doi: 10.1130/G22615.1
- 1151 von Gosen, W., Piepjohn, K., McClelland, W., & Colpron, M. (2019, 6). Evidence for
 1152 the sinistral Porcupine shear zone in North Yukon (Canadian Arctic) and geotectonic
 1153 implications. In (p. 473-491). Geological Society of America. doi: 10.1130/2019
 1154 .2541(21)
- 1155 Ward, K. M., & Lin, F. C. (2018). Lithospheric structure across the Alaskan cordillera from
 1156 the joint inversion of surface waves and receiver functions. *Journal of Geophysical
 1157 Research: Solid Earth*, 123, 8780-8797. doi: 10.1029/2018JB015967
- 1158 Woppard, G. P., Ostenso, N. A., Thiel, E., & Bonini, W. E. (1960, 3). Gravity anomalies,
 1159 crustal structure, and geology in Alaska. *Journal of Geophysical Research*, 65, 1021-
 1160 1037. Retrieved from <http://doi.wiley.com/10.1029/JZ065i003p01021> doi: 10
 1161 .1029/JZ065i003p01021
- 1162 Yang, X., Bryan, J., Okubo, K., Jiang, C., Clements, T., & Denolle, M. A. (2022b, 11). Optimal
 1163 stacking of noise cross-correlation functions. *Geophysical Journal International*,
 1164 232, 1600-1618. Retrieved from <https://academic.oup.com/gji/article/232/3/1600/6762921> doi: 10.1093/gji/ggac410
- 1165 Yang, X., & Gao, H. (2020, 11). Segmentation of the Aleutian-Alaska subduction zone
 1166 revealed by full-wave ambient noise tomography: Implications for the along-strike
 1167 variation of volcanism. *Journal of Geophysical Research: Solid Earth*, 125, 1-20. Re-
 1168 trieval from <https://onlinelibrary.wiley.com/doi/10.1029/2020JB019677> doi:
 1169 10.1029/2020JB019677
- 1170 Yang, X., Zuffoletti, I. D., D'Souza, N. J., & Denolle, M. A. (2022a, 1). *SeisGo: A ready-to-
 1171 go Python toolbox for seismic data analysis* [Computer Software]. Zenodo. Retrieved
 1172 from <https://doi.org/10.5281/zenodo.5873724> doi: 10.5281/zenodo.5873724
- 1173 Zhang, Y., Li, A., & Hu, H. (2019). Crustal structure in Alaska from receiver function
 1174 analysis. *Geophysical Research Letters*, 46, 1284-1292. doi: 10.1029/2018GL081011